

Enrichment by supernovae in globular clusters with multiple populations

Jae-Woo Lee¹, Young-Woon Kang¹, Jina Lee¹ & Young-Wook Lee²

¹*Department of Astronomy and Space Science, ARCSEC, Sejong University, Seoul 143-747, Korea*

²*Center for Space Astrophysics, Yonsei University, Seoul 120-749, Korea*

The most massive globular cluster in the Milky Way, ω Centauri, is thought to be the remaining core of a disrupted dwarf galaxy^{1,2}, as expected within the model of hierarchical merging^{3,4}. It contains several stellar populations having different heavy elemental abundances supplied by supernovae⁵ — a process known as metal enrichment. Although M22 appears to be similar to ω Cen⁶, other peculiar globular clusters do not^{7,8}. Therefore ω Cen and M22 are viewed as exceptional, and the presence of chemical inhomogeneities in other clusters is seen as ‘pollution’ from the intermediate-mass asymptotic-giant-branch stars expected in normal globular clusters⁹. Here we report Ca abundances for seven globular clusters and compare them to ω Cen. Calcium and other heavy elements can only be supplied through numerous supernovae explosions of massive stars in these stellar systems¹⁰, but the gravitational potentials of the present-day clusters cannot preserve most of the ejecta from such explosions¹¹. We conclude that these globular clusters, like ω Cen, are most probably the relics of more massive primeval dwarf galaxies that merged and disrupted to form the proto-Galaxy.

The Sejong/ARCSEC Ca uvby survey program was initiated in 2006 to investigate the homogeneous metallicity scale for globular clusters and to obtain the complete metallicity distribution function of the Galactic bulge using the hk index [= $(Ca - b) - (b - y)$]¹². The Ca filter in the hk index measures ionized calcium H and K lines, which have been frequently used to calibrate metallicity scale for globular clusters^{13,14}. The utility of the hk index is that it is known to be about three times more sensitive to metallicity than the m_1 index is for stars more metal-poor than the Sun and it has half the sensitivity of the m_1 index to interstellar reddening¹². During the last three years, we have used more than 85 nights of CTIO 1.0-m telescope time for this project. The telescope was equipped with an STA 4k \times 4k CCD camera, providing a plate scale of 0.289 arcsec/pixel and a field of view of 20 \times 20 arcmin. All of our targets accompanied with standards were observed under the photometric weather conditions and most of targets were repeatedly visited between separate runs. The photometry of our targets and standards were analyzed using DAOPHOT II, ALLSTAR, and ALLFRAME^{15,16}.

In the course of metallicity calibration of red giant branch (RGB) stars in GCs, we found that many GCs show split in the RGB in their hk versus V color-magnitude diagrams (Figs 1 and 2). The prime examples are M22 and NGC1851. In particular, the double RGB sequence in M22 is very intriguing. The differential reddening effect and the contamination from the off cluster

populations cannot explain the double RGB sequences in M22 (see Supplementary Information). It has been debated for decades whether this cluster is chemically inhomogeneous or not, but the recent high resolution spectroscopic study of 17 RGB stars in the cluster suggests that it contains chemically inhomogeneous subpopulations⁶. The bimodality in the m_1 index of M22 RGB stars was also known, but it has been argued that it is most likely due to the bimodal CN abundances, where CN absorption strengths strongly affect the m_1 index, not due to the bimodal distribution of heavy elements in the cluster¹⁷⁻¹⁹. The star-to-star light elemental abundance (C, N, O, Na, Mg and Al) variations have been known for decades and they are now generally believed to be resulted from chemical pollutions by intermediate-mass asymptotic giant branch stars⁹ or fast rotating massive stars²⁰. However, it should be emphasized that our hk measurements for RGB stars in M22, NGC1851 and other GCs show discrete or bimodal distributions in calcium abundance, which cannot be supplied by intermediate-mass asymptotic giant branch stars or fast rotating massive stars.

As shown in Fig 3, the difference in calcium, silicon, titanium and iron abundances between the calcium weak (Ca-w hereafter) group with smaller hk index and the calcium strong (Ca-s hereafter) group with larger hk index in M22 and NGC1851 suggests that they are indeed chemically distinct²¹⁻²⁴. (It is not shown in the figure but europium also has a bimodal abundance distribution in M22, in the sense that the Ca-s group has a higher europium abundance.) As for the origin of chemical inhomogeneity in globular clusters, at least four viable chemical enrichment mechanisms have been proposed up to date. They are, in the order of time required to emerge; (i) fast rotating massive stars, (ii) Type II supernovae, (iii) intermediate-mass asymptotic giant branch stars, and (iv) Type Ia supernovae. If the current understanding of supernovae explosions is correct, only Type Ia and II supernovae can supply the heavy elements such as calcium and iron¹⁰. To explain the discrete calcium abundances seen in M22 and NGC1851, however, the contribution from Type Ia supernovae can be ruled out for two reasons. First, the longer timescale ($\geq 1 - 2$ Gyr) before the onset of Type Ia supernova explosions, which would produce detectable age spread between two populations; and second, the enhanced α -elemental abundances, indicative of absence of contributions from Type Ia supernovae¹⁰. Qualitatively, the differences in elemental abundances between the two stellar populations in M22 and NGC1851 can be naturally explained by invoking chemical enrichment by Type II supernovae, where α -elements (silicon, calcium, and titanium) and r -process element (europium) are dominantly produced. However, our results do not necessarily imply that Type II supernovae are solely responsible for the chemical enrichment in M22 and NGC1851, since all four above-mentioned mechanisms may be involved. We emphasize that the crux of our results is the undeniable evidence for Type II supernovae contribution to chemical enrichment of some globular clusters, in sharp contrast to the widely accepted idea of chemical pollution only by intermediate-mass asymptotic giant branch or fast rotating massive stars, with which the chemical enhancement of the α - and r -process elements in the second generation of the stars cannot be easily explained.

More than half of 37 globular clusters in our sample shows discrete or broad distributions of the hk index in their RGB sequences. In Fig 2, We show color-magnitude diagrams for some

of exemplary globular clusters in the order of hk widths of RGB sequences at V_{HB} , the V magnitude level at the horizontal branch: ω Cen, M22, NGC1851, NGC2808, M4, M5, NGC6752 and NGC6397 (see also Supplementary Table 3 and Figs 6 – 13). NGC2808 is known to have multiple main-sequences but no multiple RGB sequences have been reported to date. Our new results show that NGC2808 shows at least two discrete RGB sequences with a large spread in calcium abundance. Similarly, M5 has very broad hk index in the RGB sequence and NGC6752 shows discrete RGB sequences. It is interesting to note that all the globular clusters with signs of multiple stellar populations have relatively extended horizontal branch, while the globular clusters with normal horizontal branch (e.g. NGC6397 in Fig 2 and Supplementary Fig 13) show no spread or split in RGB. This is consistent with the suggestion that the extended horizontal branch is a signal of the presence of multiple stellar populations in globular clusters²⁵.

The overwhelming problem of the chemical enrichment by Type II supernovae in globular clusters is that their ejecta are considered to be too energetic to be retained by less massive systems like typical Galactic globular clusters (\leq a few times $10^5 M_{\odot}$)¹¹. Our results therefore suggest that M22, NGC1851 and other globular clusters with RGB split were much more massive in the past, unless the current understanding of supernovae explosions is in great error. Perhaps, these globular clusters were once nuclei of dwarf-galaxy-like fragments and then accreted and dissolved in the Milky Way, as is widely accepted for ω Cen^{1,2,26}. Recent calculations suggest that a massive (\geq a few times $10^6 M_{\odot}$) star cluster embedded in a proto-dwarf galaxy could accrete gas from its host dwarf galaxy which may cause the formation of the second generation stars, producing multiple stellar populations²⁷. Note that this scenario is also suggesting that the globular clusters with multiple stellar populations would be the remaining cores of the proto-galactic building blocks. This idea is supported by the recent investigations of the extended horizontal branch globular clusters (i.e. globular clusters with signatures of multiple stellar populations), which has shown that extended horizontal branch globular clusters are clearly distinct from the normal globular clusters in orbital kinematics and mass²⁵. Extensive photometric surveys for fainter stars in these globular clusters, as well as spectroscopic surveys for stars in double RGB sequences, would undoubtedly help to shed more light into the discovery reported here.

1. Lee, Y. -W. *et al.* Multiple stellar populations in the globular cluster ω Centauri as tracers of a merger event. *Nature* **402**, 55–57 (1999).
2. Bekki, K. & Freeman, K. C. Formation of ω Centauri from an ancient nucleated dwarf galaxy in the young Galactic disc. *Mon. Not. R. Astron. Soc.* **346**, L11–L15 (2003).
3. Freeman, K. C. Globular clusters and nucleated dwarf elliptical. In Smith G. H & Brodie J. P. (eds) *The Globular Cluster-Galaxy Connection*. vol. 48, *Astronomical Society of the Pacific Conference Series*, 608–614 (1993).
4. Diemand, J., Kuhlen, M. & Madau, P. Formation and Evolution of Galaxy Dark Matter Halos and Their Substructure. *Astrophys. J.* **667**, 859–877 (2007).

5. Johnson, C. I. *et al.* A Large Sample Study of Red Giants in the Globular Cluster Cen (NGC5139). *Astrophys. J.* **698**, 2048–2065 (2009).
6. Marino, A. F. *et al.* A double stellar generation in the Globular Cluster NGC 6656 (M22). Two stellar groups with different iron and s-process element abundance. *Astron. Astrophys.* **505**, 1099–1113 (2009).
7. Carretta, E. *et al.* Properties of second generation stars in Globular Clusters. *ArXiv Astrophysics e-prints* (2008). arXiv:astro-ph/0811.3591v1.
8. Georgiev, I. Y. *et al.* Globular cluster systems in nearby dwarf galaxies II. Nuclear star clusters and their relation to massive Galactic globular clusters. *Mon. Not. R. Astron. Soc.* **396**, 1075–1085 (2009).
9. Ventura, P. D. *et al.* Predictions for self-pollution in globular cluster stars. *Astrophys. J. Lett* **550**, L65–L69 (2001).
10. Timmes, F. X., Woosley, S. E. & Weaver, T. A. Galactic Chemical Evolution: Hydrogen through Zinc. *Astrophys. J. Suppl.* **98**, 617–658 (1995).
11. Baumgardt, H., Kroupa, P. & Parmentier, g. The influence of residual gas expulsion on the evolution of the Galactic globular cluster system and the origin of the Population II halo. *Mon. Not. R. Astron. Soc.* **384**, 1231–1241 (2008).
12. Anthony-Twarog, B. J. *et al.* Ca II H and K filter photometry on the uvby system. I-The Standard system. *Astron. J.* **101**, 1902–1914 (1991).
13. Zinn, R. The globular cluster system of the Galaxy. I. The metal abundances and reddening of 79 globular clusters from integrated light measurements. *Astrophys. J. Suppl.* **42**, 19–40 (1980).
14. Zinn, R. & West, M. J. The globular cluster system of the Galaxy. III. Measurements of radial velocity and metallicity for 60 clusters and a compilation of metallicities for 121 clusters. *Astrophys. J. Suppl.* **55**, 45–66 (1984).
15. Stetson, P. B. DAOPHOT A computer program for crowded-field stellar photometry. *Publ. Astron. Soc. Pacif.* **99**, 191–222 (1987).
16. Stetson, P. B. The center of the core-cusp globular cluster M15: CFHT and HST observations, ALLFRAME reductions. *Publ. Astron. Soc. Pacif.* **106**, 250–280 (1994).
17. Norris, J. & Freeman, K. C. The chemical inhomogeneity of M22. *Astrophys. J.* **266**, 130–143 (1983).
18. Richter, P., Hilker, M. & Richtler, T. Strömgren photometry in globular clusters: M55 & M22. *Astron. Astrophys.* **350**, 476–484 (1999).

19. Anthony-Twarog, B. J., Twarog, B. A. & Craig, J. CN and Ca abundance variations among the giants in M22. *Publ. Astron. Soc. Pacif.* **107**, 32–48 (1995).
20. Decressin, T., Charbonnel, C. & Meynet, G. Origin of the abundance patterns in Galactic globular clusters: constraints on dynamical and chemical properties of globular clusters. *Astron. Astrophys. J.* **475**, 859–873 (2007).
21. Yong, D. & Grundahl, F. An abundance analysis of bright giants in the globular cluster NGC1851. *Astrophys. J. Lett.* **672**, L29–L32 (2008).
22. Lee, J. -W. *et al.* Chemical inhomogeneity in red giant branch stars and RR Lyrae variables in NGC1851: Two subpopulations in red giant branch. *Astrophys. J. Lett.* **695**, L78–L82 (2009).
23. Cudworth, K. M. Proper motions, membership, and photometry in the globular cluster M22. *Astron. J.* **92**, 348–357 (1986).
24. Brown, J. A. & Wallerstein, G. High-resolution CCD spectra of stars in globular clusters. VII. Abundances of 16 elements in 47 Tuc, M4, and M22. *Astron. J.* **104**, 1818–1830 (1992).
25. Lee, Y. -W., Gim, H. B. & Casetti-Dinescu, D. Kinematic decoupling of globular clusters with the extended horizontal branch. *Astrophys. J. Lett.* **661**, L49–L52 (2007).
26. Piotto, G. *et al.* Metallicities on the Double Main Sequence of ω Centauri Imply Large Helium Enhancement. *Astrophys. J.* **621**, 777–784 (2005).
27. Pflamm-Altenburg, J. & Kroupa, P. Recurrent gas accretion by massive star clusters, multiple stellar populations and mass threshold for spherical stellar systems. *Mon. Not. R. Astron. Soc.* **397**, 488–494 (2009).

Supplementary Information is linked to the online version of the paper at www.nature.com/nature.

Acknowledgements J.-W. L. thanks A. Walker for providing the CTIO Ca filter transmission curve, D. Yong for NGC1851 spectroscopic data before publication and A. Yushchenko for discussions on spectrum synthesis. Support for this work was provided by the National Research Foundation of Korea to the Astrophysical Research Center for the Structure and Evolution of the Cosmos (ARCSEC). This work was based on observations made with the CTIO 1.0-m telescope, which is operated by the SMARTS consortium.

Author Contributions J.-W. L. performed observations, data analysis, interpretation, model simulations and writing of the manuscript. Y.-W. K. participated in observation planning, J. L. performed a part of observations and data analysis. Y.-W. L. performed interpretation and writing of the manuscript. All authors discussed the results and commented on the manuscript.

Author Information Reprints and permissions information is available at www.nature.com/reprints. The authors declare that they have no competing financial interests. Correspondence should be addressed to J.-W. L. (jaewoolee@sejong.ac.kr) or Y.-W. L. (ywlee2@yonsei.ac.kr).

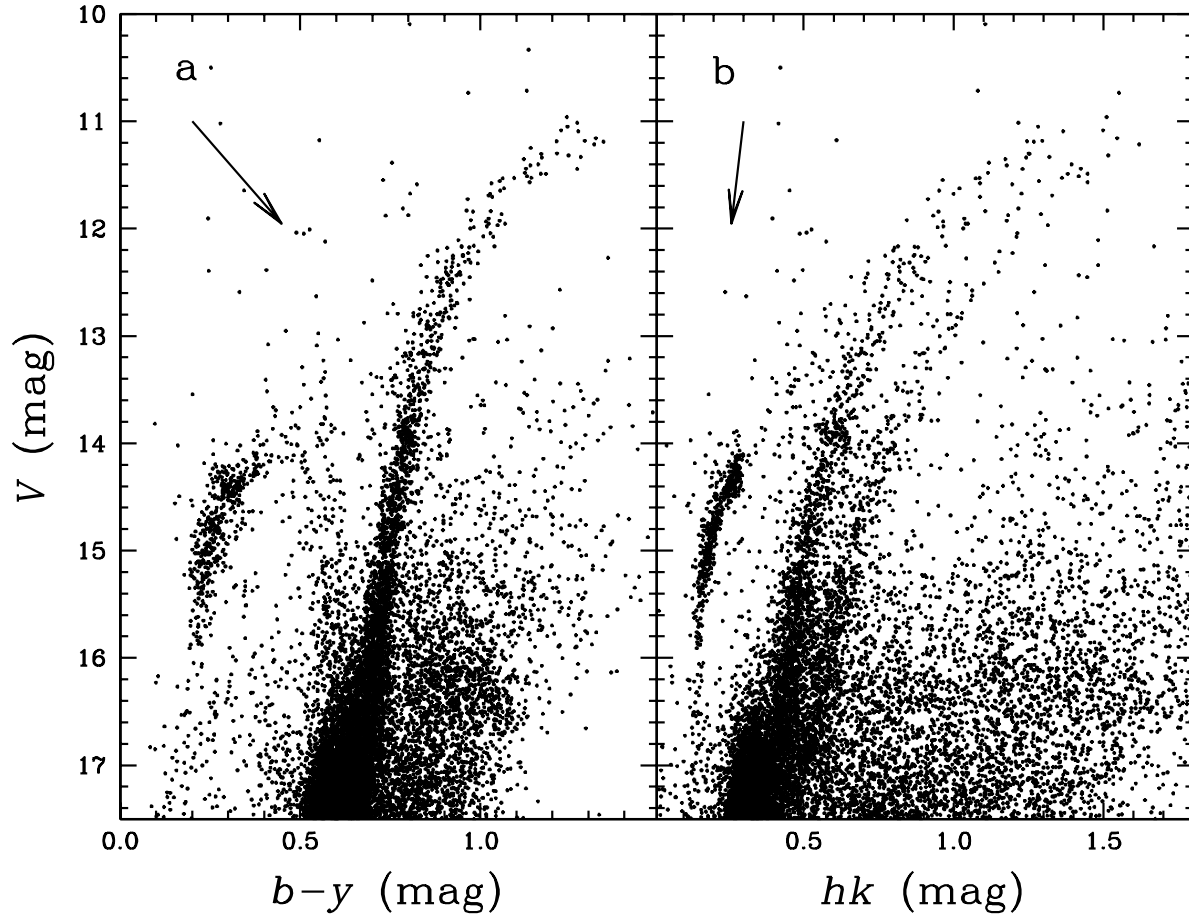


Figure 1: **Color-magnitude diagrams for M22.** **a**, V versus $b - y$; **b**, V versus hk . In **b**, note the distinct and discrete double RGB sequences in M22. This cannot be due to differential reddening effect across the cluster or the contamination from the off cluster field but, is due to the difference in calcium abundance, which was synthesized in supernovae, between the two RGB sequences. The number ratio between the Ca-w group with smaller hk index and the Ca-s group with larger hk index is about 70:30. Black arrows in each panel denote reddening vectors.

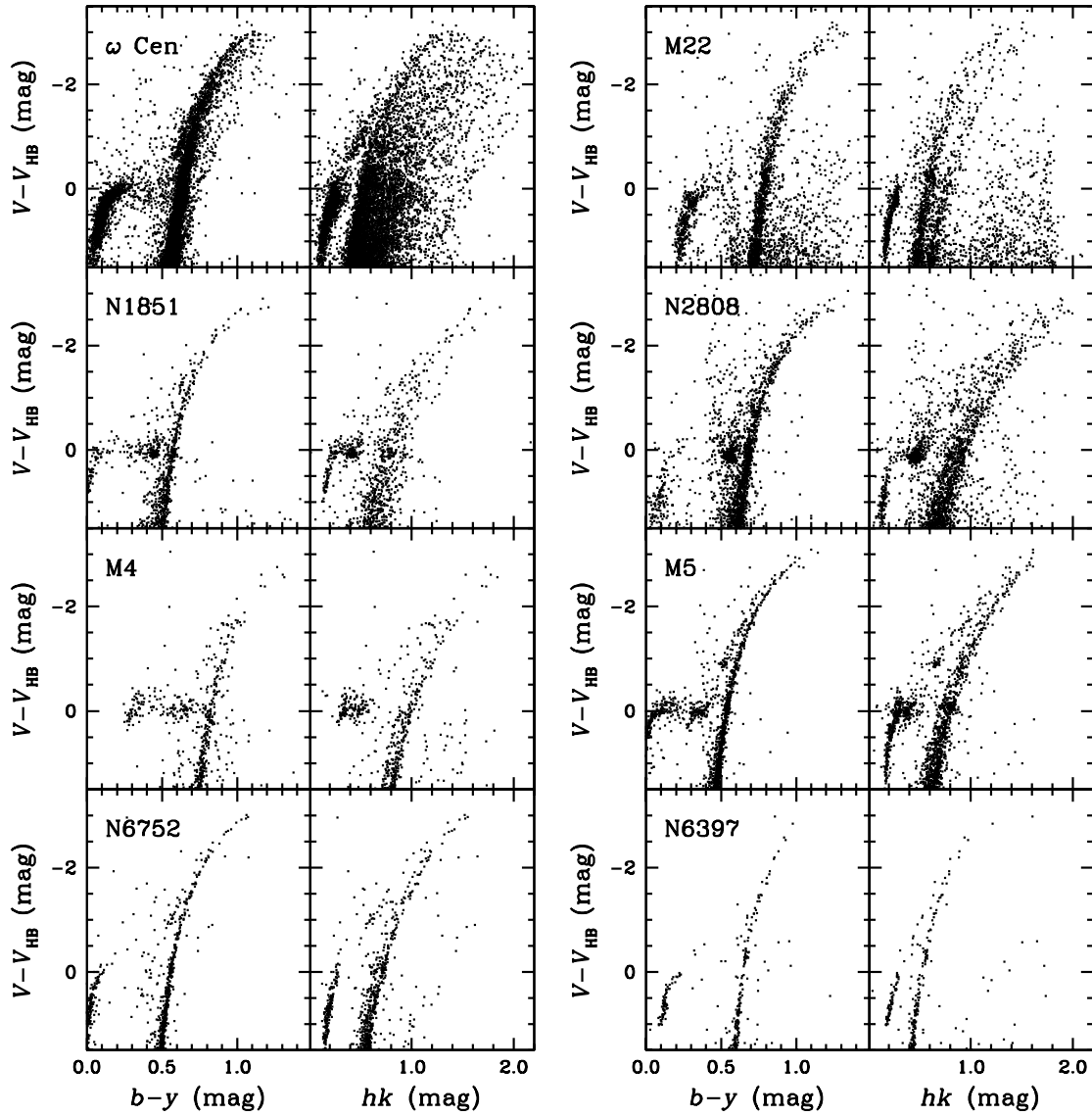


Figure 2: **Color-magnitude diagrams for ω Cen, M22, NGC1851, NGC2808, M4, M5, NGC6752 and NGC6397.** Note that, while the distributions of the RGB sequences in the $b - y$ color are relatively narrow, those in the hk index are either discrete or broad. This is evidence for the multiple stellar populations with distinct calcium abundances. Among these globular clusters, NGC6397 appears to be the only normal globular cluster with simple population (i.e. coeval and monometallic).

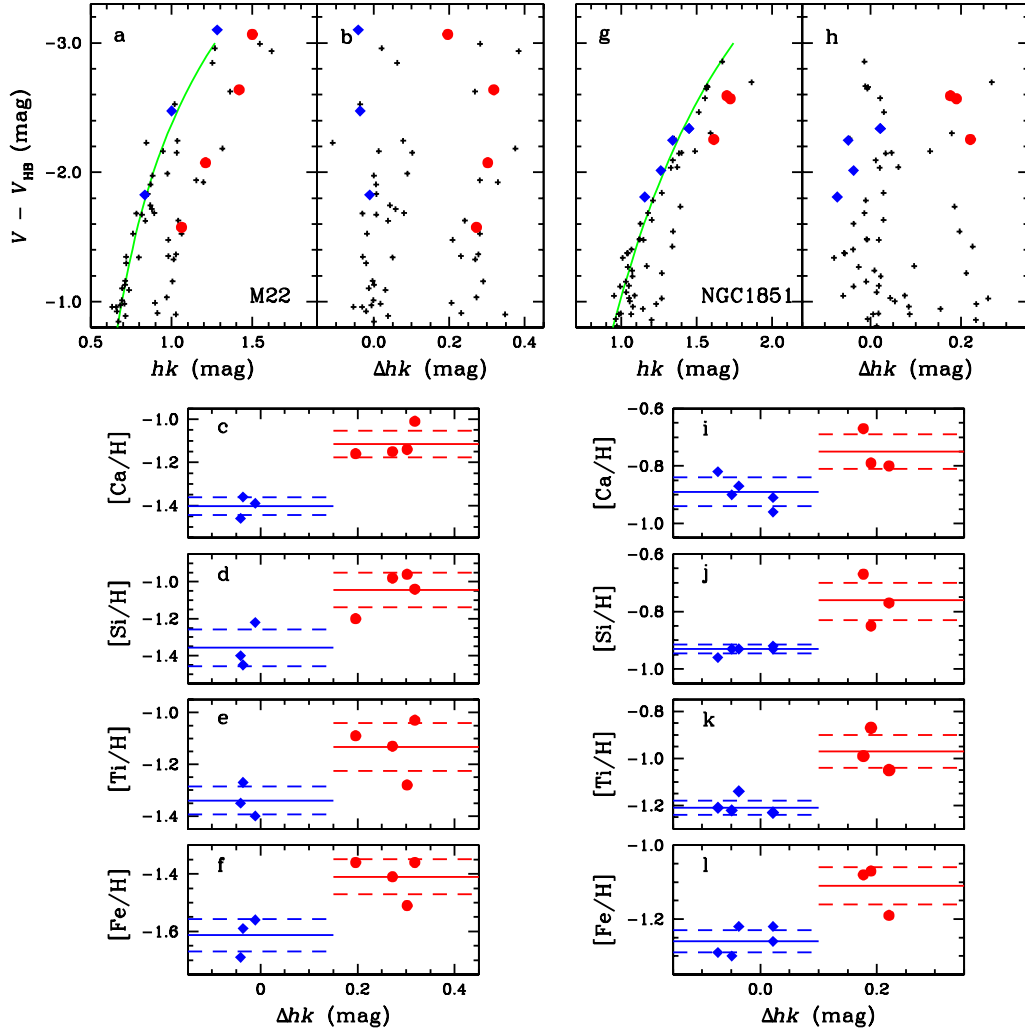


Figure 3: **Differences in chemical compositions between double RGB sequences in M22 and NGC1851.** **a, b**, Black ‘plus’ signs denote stars in M22 with proper motion membership probabilities $P \geq 90\%$; blue filled diamonds and red filled circles denote RGB stars studied with high-resolution spectroscopy in the Ca-w and the Ca-s groups, respectively^{23,24}. The green solid line denotes the fiducial sequence of RGB stars and Δhk denotes the difference in the hk index against the fiducial sequence. The double RGB sequences persist in proper motion member stars. **c – f**, Comparisons of elemental abundances between the Ca-w and the Ca-s groups in M22. Solid lines denote the mean values, and dashed lines denote standard deviations of each group. The Ca-s group has higher α -elements (Si, Ca, and Ti) and iron abundances, which must be supplied by numerous Type II supernova explosions. **g, h**, Black ‘plus’ signs denote stars in NGC1851; blue filled diamonds and red filled circles denote RGB stars studied with high-resolution spectroscopy in the Ca-w and the Ca-s groups, respectively^{21,22}. **i – l**, As **c – f** but for NGC1851.

Supplementary Information

1 The CTIO Ca Filter System

The Filter Transmission The Ca filter system was designed to include Ca II H and K lines at λ 3968 and 3933 Å, respectively, with a full-width half maximum (FWHM) of approximately 90 Å. The CN band absorption strengths at $\approx \lambda$ 3885 Å are often very strong in stellar spectra and the lower limit of the Ca filter is set to avoid contamination by the CN band¹². The Ca filter used at Cerro Tololo Inter-American Observatory (CTIO) has a similar FWHM, approximately 90 Å, but its passband is shifted approximately 15 Å to the longer wavelength (Alistair Walker, private communication) compared to that in Anthony-Twarog *et al.*¹² In Supplementary Figure 1, we show the transmission functions of the both Ca filters. In the figure, we also show synthetic spectra for the CN normal and the CN strong RGB stars in typical intermediate metallicity globular clusters (GCs) as an illustration. The effect of the CN band on the hk index is negligible as will be discussed below.

The Central Wavelength Drift of the Ca Filter The CTIO Ca filter transmission function shown in Supplementary Figure 1 is that measured with a collimated beam. It is known that the passband of the narrow band interference filter depends on the angle of the incidence beam following,

$$\lambda = \lambda_0 \left(1 - \frac{\sin^2 \beta}{n^{*2}} \right)^{1/2}, \quad (1)$$

where λ_0 is the wavelength of peak transmittance at normal incidence, β is the angle of incidence of the collimated beam on the filter and n^* is the effective refractive index of the filter²⁸. Therefore, when the Ca filter is used with a fast telescope, the filter passband can be significantly different from that shown in Supplementary Figure 1. The CTIO 1-m telescope used for our survey is a slow telescope with $f/10.5$ and the effect resulted from the angular dependency of a converging beam is expected to be very small. Assuming $\beta \approx 1/21$ radians for the converging beam at the CTIO 1-m telescope and $n^* \approx 1.4$ for the CTIO Ca filter, the peak wavelength of the Ca filter will be shifted by 2.3 Å to the shorter wavelength. Given the much larger FWHM of the CTIO Ca filter, this may contribute small effect. We investigate contributions to the hk index resulted from the shifted Ca passband using synthetic spectra for typical intermediate metallicity RGB stars in our GCs. Our calculations integrating over the filter transmission curve show that this effect contributes no larger than 0.011 mag to our hk measurements, in the sense that the shifted Ca passband to the shorter wavelength gives slightly larger hk values. We emphasize that, since our results are based on a single instrument setup (the same telescope, filters and the CCD camera) during the observations of our science targets and the photometric standards, this effect is expected to be cancelled out during our photometric calibrations. Also importantly, our main results presented here rely on the split or the spread in the hk index of RGB stars of an individual GC. Therefore, the shifted Ca passband affects similar degree to the hk index of the RGB stars in a GC and does not contribute to the apparent RGB split or the spread in the hk index of an individual GC.

Effect of radial motions and internal velocity dispersions of GCs The mean radial motion of 139 GCs in our Milky Way Galaxy²⁹ is $|v_r| = 110$ km/s, equivalent to the wavelength shift by $|\Delta\lambda| \approx 1.4 \text{ \AA}$ at $\lambda 3950\text{\AA}$. We calculate the contribution due to the mean radial motion of GCs to the hk index using the shifted CTIO Ca passband and synthetic spectra for typical intermediate metallicity GC RGB stars. We find that the net effect is negligibly small, $|\Delta hk| < 0.006$ mag. Among our eight GCs, NGC1851 has the largest radial velocity, $v_r = 321$ km/s, equivalent to the wavelength shift by $\Delta\lambda = 4.2 \text{ \AA}$ to the longer wavelength at $\lambda 3950\text{\AA}$. We calculate the contribution due to the radial motion of NGC1851 using the shifted CTIO Ca passband and the red-shifted synthetic spectra with a fixed CN abundance for the cluster. We obtain $\Delta hk \approx 0.015$ mag, in the sense that the red-shift is resulted in a slightly larger hk index. As we discussed above, the difference in the hk index due to the high radial motion of NGC1851 does not affect our results presented here, since the hk indices of RGB stars in NGC1851 will be affected by similar degree and the mean radial motion of the cluster does not produce an apparent split or a spread in the hk index. Perhaps, this effect may become important in the inter-cluster comparisons, which is beyond the scope of our study.

What concerns us most about the high radial velocities of some GCs, in particular for red-shift, is the potential contamination by the strong CN band absorption features at $\lambda 3885 \text{ \AA}$ as shown in Supplementary Figure 1. For example, NGC1851 has a bimodal CN distribution and some RGB stars show very strong CN band absorption strengths³⁰. Due to its high radial velocity away from us (i.e. red-shifted), the CN band absorption features in the CN-strong RGB stars may affect the hk index and, subsequently, may produce an apparent RGB split of the cluster as shown in Figure 2 or Supplementary Figure 8. We calculate the CN band contributions using the shifted CTIO Ca passband and the red-shifted synthetic spectra for the CN-normal and the CN-strong RGB stars (see discussion below). Our calculations suggest that the net effect is negligibly small, $\Delta hk \leq 0.003$ mag, and the high radial velocity of NGC1851 combined with a bimodal CN distributions does not produce the RGB split in the hk index.

We also investigate the effect of the internal velocity dispersion of an individual GC. Assuming $\sigma_{LOS} = 15$ km/s, equivalent to $\Delta\lambda \leq 0.2 \text{ \AA}$ at $\lambda 3950\text{\AA}$, we obtain $\Delta hk \leq 0.001$ mag following the same method described above, and the effect from the internal velocity dispersions of GCs does not affect our results.

Summary of uncertainties on the hk index Supplementary Table 1 summarizes the uncertainties in our hk index measurements relevant to the CTIO Ca passband. (The variations in the hk index due to differences in elemental abundances of GC RGB stars will be discussed below.) As discussed above, the effects due to the shifted CTIO Ca passband and the radial motions of GCs do not affect our results, since both effects contribute similar degree to the hk indices among RGB stars in a GC. (i.e. They only affect the zero point of the hk index and they do not affect the Δhk distributions). In addition to our photometric measurement errors which will be discussed below, the effects due to the internal velocity dispersions of GCs and the differential interstellar Ca II absorption (see discussion below) can affect our hk index measurements. However, their con-

tributions to our hk measurements are no larger than 0.022 mag and they do not affect our main conclusion presented here. Therefore, our results strongly suggest that the split or the spread in the hk index of RGB stars in GCs are related to the variations in elemental, in particular calcium, abundances among RGB stars in a GC, which will be discussed below.

2 The Double RGB Sequences of M22

Differential Reddening Effect on the Double RGB Sequences in M22 The continuous interstellar extinction by the interstellar dust and the discrete interstellar line extinction by the interstellar Ca II atoms may affect our main results. We considered both effects and will discuss that the RGB split of M22 in the hk index is indeed due to the difference in calcium abundances between two stellar populations in M22 and other explanations are highly unlikely. Also both effects tend to produce spreads in RGB sequences rather than the distinct and discrete RGB sequences of GCs reported here.

The differential continuous reddening across the cluster can thicken the apparent RGB sequence of GCs in broad-band optical photometry³¹. In contrast to other color indices being used in broad-band photometry, the hk index is known to be insensitive to interstellar reddening¹², $E(hk)/E(b-y) = -0.16$ and $E(hk)/E(B-V) = -0.12$. The difference in the hk index between the two RGB sequences in M22 is about 0.2 mag at the magnitude level of the horizontal branch. If this hk split is only due to differential reddening effect, we would expect even larger separation of the two RGB sequences in the $b-y$ color and the V magnitude. The reddening correction value in the $b-y$ color, $E(b-y)$, for the Ca-s group is about -1.25 mag, equivalent to $E(B-V) = -1.69$ mag assuming $E(b-y)/E(B-V) = 0.74$, making the RGB stars in the Ca-s group too hot to be RGB stars (see Supplementary Figure 2 – d). At the same time, the extinction correction value in the V magnitude is -5.24 mag, assuming $A_V = 3.1 \times E(B-V)$, for the Ca-s RGB stars. Applying this large extinction correction makes the RGB stars in the Ca-s group too bright to be members of M22 (see Supplementary Figure 2 – e & f). We emphasize that both the Ca-w and the Ca-s groups are proper motion members of the cluster as shown in Figure 3. Note also that the reddening vector (see Figure 1 or Supplementary Figure 4) is almost parallel to the slopes of HB and RGB in the hk versus V CMD, and thus the differential reddening can not produce the RGB split. Therefore, continuous differential reddening effect can be completely ruled out to explain the observed bimodal RGB sequences in M22. Similarly, the interstellar reddening toward NGC1851 is very small, $E(B-V) = 0.02$ mag²⁹, but the hk split in RGB stars of the cluster is as large as 0.2 mag (see Supplementary Figure 8), which can not be explained by differential continuous reddening effect²².

The previous study for the GCs showed that the equivalent width of the interstellar Ca II K absorption line strength can be as large as several times $100 \text{ m}\text{\AA}$ ³². The interstellar Ca II atom is thought to be heavily depleted on to dust in denser clouds³³, which may cause small-scale differential discrete reddening effect across M22 and other GCs studied here (see also Andrew *et al.*³⁴

for the small-scale variations of interstellar Na I D lines¹ toward the less extinguished globular cluster M92). We generate synthetic spectrum to surrogate interstellar Ca II H & K absorption lines. We adopt a gaussian line profile with a FWHM of 1 Å, equivalent to $\Delta v_r \approx 76$ km/s, and we assign equivalent widths of 350 mÅ and 650 mÅ for the interstellar Ca II H & K lines, respectively. Our synthetic spectrum is shown in Supplementary Figure 1 – (c). Assuming they are linear part of the curve of growth³⁵, the column density of the interstellar Ca II can be estimated as

$$N(\text{Ca II}) = 1.13 \times 10^{20} \frac{EW}{\lambda^2 f}, \quad (2)$$

where EW and λ are the equivalent width and wavelength in Å and f is the oscillator strength. Using the oscillator strengths of 0.681 and 0.341 for Ca II H & K, respectively, the column density for interstellar Ca II is $\log N(\text{Ca II}) \approx 12.8 \text{ cm}^{-2}$, equivalent to $\Delta E(B - V) \approx 0.32 \text{ mag}$ ³³. If this large amount of small-scale interstellar Ca II variation exists among our GCs studied here, how much will it affect our hk index measurements? We calculate the Ca magnitudes with and without the interstellar Ca II variations using the shifted CTIO Ca transmission function. The difference in the Ca magnitude (i.e. in the hk index since the interstellar Ca II H & K lines do not affect b or y passbands) is only 0.010 mag and, therefore, the differential discrete reddening effect due to the variations in the interstellar Ca II abundances can be completely ruled out to explain the GC RGB splits in the hk index.

The Spatial Distributions In Supplementary Figure 3, we show the spatial distributions of Ca-w and Ca-s RGB stars in M22. As can be seen in the figure, each population does not show any spatially patched features, supporting our results that differential reddening is not responsible for the RGB split in M22.

Contamination from the Milky Way’s Bulge Population M22 is located in the direction of the Milky Way’s bulge and the contamination from the bulge population may affect our results. However, this is very unlikely, since the proper motion member RGB stars show discrete double RGB sequences as shown in Figure 3. In addition, the bulge RGB stars are located farther from the Sun, more metal-rich and suffering from heavier interstellar reddening than those in M22 are. In Supplementary Figure 4, we compare M22 CMDs with those of two bulge fields (NGC6528 and OGLEII - 12). As can be seen in the figure, the RGB stars in the bulge are fainter and redder than those in M22 are and the contamination from the Milky Way’s bulge population does not affect our results.

Effects of Metal Contents and Helium Abundances on the M22 RGB As shown in Figure 3, the stars in the Ca-s group are about 0.2 dex more metal-rich than those in the Ca-w group. It is suspected that this large metallicity spread may produce any detectable discrepancy in stellar evolutionary sequences, in particular for RGB sequence, between two stellar populations based

¹Note that the number of interstellar Na I atoms appears to be about a factor of ten larger than that of interstellar Ca II atoms³³.

on broad-band photometry. To explore metallicity effect on the RGB sequence, we compare BV CMD by Monaco *et al.*³¹ with the latest Y^2 isochrones (Version 3, Yi *et al.* in preparation). In Supplementary Figure 5, we show model isochrones for $[\text{Fe}/\text{H}] = -1.6$ and -1.4 with the helium abundance of $Y = 0.23$ and the age of 11 Gyr, using the reddening value and the distance modulus for the cluster from Harris²⁹. Although the split in the RGB sequences of two model isochrones is noticeable, the discrepancy in the RGB sequence does not appear to cause a serious problem to explain the BV CMD by Monaco *et al.*³¹ Note that the V magnitude difference in the sub-giant branch between two model isochrones can be as large as 0.2 mag, apparently consistent with recent HST/ACS observations of the cluster³⁶.

As inferred from the extended HB (EHB) morphology of M22, the second generation of the stars is expected to have enhanced helium abundance by $\Delta Y \approx 0.05$ ³⁷. Since the new version of Y^2 isochrones provides models with enhanced helium abundances, we investigate the effect of helium abundance on the evolutionary sequence. As illustrated in Supplementary Figure 5 – (c), the discrepancy between two stellar populations alleviates due to the opposite effect of metal contents and helium abundances on the RGB temperature. Since the second generation of the stars in M22 shows signs of the chemical enrichment by Type II supernovae and intermediate-mass asymptotic giant branch (AGB) stars, the second generation of stars may be slightly younger than the first generation. Assuming the age difference of 1 Gyr between two stellar populations, two model isochrones are in excellent agreement except for bright RGB sequence, where the observed number of stars is small.

It is intriguing to note that the number ratio between the Ca-w and the Ca-s RGB stars (70:30) found here is very similar to those found between (1) the two stellar groups with different $[\text{Fe}/\text{H}]$ and $[s\text{-process}/\text{Fe}]$ ratios⁶, (2) the brighter SGB and the fainter SGB stars³⁶, and (3) the two groups of HB stars with the bluer HB being less populated. The population synthesis models (Han *et al.* 2009, in preparation) suggest that this can be naturally reproduced by the enhanced metal and helium abundances in the second generation of stars.

3 The hk and Metallicity Distributions of GCs

Observations In Supplementary Table 2, we show the journal of observations for eight GCs. They were observed under the photometric weather conditions and, for most cases, the median seeing was about 1.5 – 1.6 arcsec during our observations. Note that the RGB stars in NGC2808 are roughly 21 times fainter than those in NGC6397 in the Ca passband for a fixed magnitude, while our total integration time for NGC2808 is only about three times longer than that for NGC6397 in the Ca passband. Statistically, the lack of total integration time for NGC2808 will be resulted in a ≈ 2.6 times larger Ca measurement error than that expected for NGC6397 at a given Ca magnitude, particularly for fainter stars. Although our survey relied on a rather small telescope through a rather

narrow filter at a rather blue wavelength², our investigations of the multiple stellar populations of GCs are focused on bright RGB stars, where the numbers of photon in the Ca passband are enough so that the measurement errors, including propagation errors during the photometric calibrations, are less than 0.020 mag (see Supplementary Table 3).

Color Distributions of Bright RGB Stars Here, we investigate the $b - y$ color and the hk index distributions of RGB stars brighter than $V - V_{\text{HB}} = 1.0$ mag. We derive lower order ($\approx 4 - 5$) polynomial fits, which are forced to pass through the peak $b - y$ colors or the peak hk indices of given magnitude bins, as fiducial sequences for eight GCs and then we calculate differences in the $b - y$ color, $\Delta(b - y)$, or the hk index, Δhk , with respect to fiducial sequences of each GC. We show our results in Supplementary Figures 6 – 13. In the figures, the blue horizontal bars denote the mean measurement errors including propagation errors during the photometric calibrations with a $2\sigma_*$ range ($\pm 1\sigma_*$) for individual stars at given magnitude bins.

In Supplementary Table 3, we show comparisons of the observed FWHMs of RGB stars and the measurement errors at the magnitude level of horizontal branch stars, $V_{\text{HB}} + 0.5 \geq V \geq V_{\text{HB}} - 0.5$, in each GC. To calculate the FWHMs of RGB stars in GCs, we used the following relation,

$$\text{FWHM}(\text{RGB}) \approx 2.3548 \times \sigma_{\Delta}, \quad (3)$$

where σ_{Δ} is the standard deviation of RGB stars in the $\Delta(b - y)$ or the Δhk distributions in a fixed magnitude bin. Note that the FWHM of RGB stars in the hk index is slightly larger than the hk separation between the double populations such as in M22, NGC1851, NGC2808, M4 and NGC6752. The mean measurement errors, $\sigma_*(b - y)$ or $\sigma_*(hk)$, given in the table include propagation errors during the photometric calibrations and they are those for individual stars. Therefore, the mean measurement errors for an individual population in GCs, $\sigma_p(b - y)$ or $\sigma_p(hk)$, will be given by $\approx \sigma_*(b - y)/\sqrt{n_p}$ or $\sigma_*(hk)/\sqrt{n_p}$, where n_p (≥ 20) is the number of stars in each population. Note that, while the FWHMs of most GCs have much larger values [$\geq 8\sigma_*(hk)$] than the measurement errors for individual stars in the hk index, the FWHM of NGC6397 is comparable in size to the measurement error in the hk index, consistent with the idea that NGC6397 is the only normal GC with a simple stellar population (i.e. coeval and monometallic) in our sample. Also note that NGC6397 shows similar degree of the full RGB widths in the $\Delta(b - y)$ and the Δhk distributions (see Supplementary Table 3 and Supplementary Figure 13).

The last two columns of Supplementary Table 3, $E(b - y)_{1/2}$ and $E(hk)_{1/2}$, are for the contributions due to the continuous differential reddening effect assuming a 50% variation in the total interstellar reddening across each GC. The observed FWHMs of GCs in the $(b - y)$ color and in the hk index can not be explained simultaneously, similar to what shown in Supplementary Figure 2. Therefore, the continuous differential reddening effect can be ruled out to explain the

²Fortunately, the CCD camera used in our survey has rather high quantum efficiency (QE) at shorter wavelength with QE ≈ 0.686 at λ 3800Å and ≈ 0.770 at λ 4000Å. (see <http://www.astronomy.ohio-state.edu/Y4KCam/OSU4K/index.html#DQE>).

differences between the observed FWHMs(RGB) and the measurement errors in GCs.

Δhk as a probe of multiple stellar populations in GCs For ω Cen, M22 and NGC1851 (see Figure 3 and Supplementary Figure 15), when the two subpopulations are defined by our hk index (or our Δhk distribution), we can also see the clear division in spectroscopic elemental abundances. Similarly, we will discuss that the split or the spread in the Δhk distributions of RGB stars in other clusters can provide a powerful method to probe the multiple stellar populations in GCs.

The calcium abundance is the major factor that determines the hk index or the Δhk distribution of RGB stars in a GC (see discussion below) and Type II supernovae are responsible for the calcium enrichment in a GC. As discussed, however, our results do not imply that Type II supernovae are solely responsible for the chemical enrichment in GCs. In an attempt to explain the observed large star-to-star lighter elemental abundance variations (in particular O and Na) in GCs, chemical pollution by intermediate mass AGB stars⁹ or fast rotating massive (FRM) stars²⁰ has been widely accepted. It should be reminded that, however, neither AGB nor FRM scenarios can explain the chemical enrichment of the α - and r -process elements in the second generation of the stars. It is most likely that all three aforementioned mechanisms (and perhaps including Type Ia supernovae) are required to explain elemental abundance patterns found in GCs. In addition to the chemical enrichment by Type II supernovae, which is the main results presented here, if the second generation of the stars in some of our GCs have experienced the chemical pollution by intermediate-mass AGB or FRM stars, the lighter elemental abundances, such as oxygen and sodium, between the two generations of stars must have been different. Furthermore, the variations in [O/Fe] and [Na/Fe] can be as large as 1 dex in some GCs⁷ and the differences in the oxygen and sodium abundances are easily detectable compared to those in the heavy elements, such as calcium and iron.

During the last few years, tremendous amount of effort has been directed at spectroscopic study of RGB stars in GCs, in particular, using the multi-object spectrograph mounted at VLT. Among our eight GCs, NGC2808³⁸, M4³⁹ and NGC6752⁴⁰ have been studied using moderately high resolution spectra for more than 100 RGB stars. In Supplementary Figure 14, we show comparisons of Δhk versus O, Na and Fe distributions of the clusters. In panel (a), we show the plot of $V - V_{\text{HB}}$ versus Δhk for NGC2808 RGB stars. In the figure, the plus signs denote the RGB stars with known [O/Fe] and [Na/Fe] ratios³⁸. From the Δhk distribution of RGB stars shown in panel (b), we define the boundary at $\Delta hk = -0.05$ mag (the vertical dashed line) assuming that NGC2808 has two major stellar populations as shown in panel (b) or Supplementary Figure 9. Similar to the procedure employed in M22 and NGC1851 (see Figure 3), we define the Ca-w group with smaller hk index and the Ca-s group with larger hk index and they are denoted by the blue and the red plus signs, respectively, in panel (a). In panels (c), (d) and (e), we show the [O/Fe], [Na/Fe] and [Fe/H] distributions for each group, where the shaded histograms outlined with blue color are for the Ca-w group and the blank histograms outlined with red color are for the Ca-s group. The Ca-w group has a higher mean oxygen and a lower mean sodium abundances, while the Ca-s group has a lower mean oxygen and a higher mean sodium abundances, indicative of

the presence of the proton-capture process at high temperature between the two formation epochs presumably via intermediate-mass AGB or FRM stars, where oxygen is depleted by the CNO cycle while sodium is enriched from the $^{22}\text{Ne} + ^1\text{H} \rightarrow ^{23}\text{Na}$ reaction. Our results strongly suggest that they are truly different stellar populations and not related to, for example, our photometric measurement errors and differential reddening effect: the Ca-w group is the first generation of stars while the Ca-s group is the second generation of stars enriched by Type II supernovae (e.g. calcium) and intermediate-mass AGB or FRM stars (e.g. sodium). Although the difference in the [Fe/H] distributions between the two groups does not appear to be as compelling as those in the [O/Fe] and the [Na/Fe] distributions, the Ca-w group has a slightly lower mean metallicity than the Ca-s group does. We performed non-parametric Kolmogorov-Smirnov (K-S) tests to see if the [Fe/H] distributions of the two populations in NGC2808 are drawn from the same parent population. Our calculation shows that the probability of being drawn from identical stellar populations is 5.5% for NGC2808, suggesting that they have different parent populations.

The same results can be found in M4 and NGC6752. From the comparisons of the [O/Fe] and the [Na/Fe] distributions between the Ca-w and the Ca-s groups, it can be seen that the Ca-w groups are the first generations of stars while the Ca-s groups are the second generations of stars in the clusters. We also performed K-S tests for the [Fe/H] distribution of M4, we obtained that the probability of being drawn from identical parent populations is 5.5% for M4, indicating that each subpopulation in M4 has different parent populations.

Recalibration of $[\text{Fe}/\text{H}]_{hk}$ Based on RGB Stars in ω Cen and Metallicity Distributions of Eight GCs In our previous study for NGC1851, we showed that the hk index traces the calcium abundance and, furthermore, it can provide a very powerful method to distinguish multiple stellar populations in GCs²². However, it can be seen that the full range of Δhk increases with the luminosity of RGB stars (i.e. different temperature or surface gravity), in particular, in ω Cen and M22. Due to the temperature dependency on the hk index versus metallicity relation, the Δhk distributions cannot be directly translated into the absolute metallicity scale. Therefore, we calculate the photometric metallicity, $[\text{Fe}/\text{H}]_{hk}$, of individual RGB stars in eight GCs using the [Fe/H] relations on the hk_0 versus $(b - y)_0$ plane^{12,22}.

Recently, Johnson *et al.*⁵ studied elemental abundances, including calcium, of large sample of RGB stars in ω Cen using moderately high resolution spectra ($R \approx 18,000$). Since ω Cen contains multiple stellar populations with very broad metallicity range, $\Delta[\text{Fe}/\text{H}] \approx 1.5$ dex, comparisons of our results of RGB stars in ω Cen with those of Johnson *et al.* may provide an wonderful opportunity to assess our photometric metallicity scale using the hk index, $[\text{Fe}/\text{H}]_{hk}$. In Supplementary Figure 15, we show elemental abundances of 40 RGB stars in ω Cen studied by Johnson *et al.* as a function of Δhk . As shown in the figure, [Ca/H] and [Fe/H] appear to be well correlated with Δhk , indicating that Δhk can truly be treated as the relative calcium abundance or metallicity indicators for RGB stars with similar luminosities in a GC. We also show plots of $[\text{Fe}/\text{H}]_{\text{spec}}$ versus $[\text{Fe}/\text{H}]_{hk}$ and $[\text{Ca}/\text{H}]_{\text{spec}}$ versus $[\text{Fe}/\text{H}]_{hk}$ for 32 RGB stars with sufficiently high

signal-to-noise ratios (≥ 100). We derive linear fits to each relation and we find

$$[\text{Fe}/\text{H}]_{\text{spec}} = 0.533[\text{Fe}/\text{H}]_{\text{hk}} - 0.775 \quad (\sigma = 0.087\text{dex}), \quad (4)$$

and

$$[\text{Ca}/\text{H}]_{\text{spec}} = 0.587[\text{Fe}/\text{H}]_{\text{hk}} - 0.403 \quad (\sigma = 0.106\text{dex}). \quad (5)$$

We recalibrate our photometric metallicity using the equation (4), $[\text{Fe}/\text{H}]_{\text{hk},\text{corr}}$, and we derive metallicity distribution functions (MDFs) for eight GCs. During our calculations of MDFs, we use RGB stars with $-2.0 \leq V - V_{\text{HB}} \leq -0.5$ mag in order to minimize contamination from off-cluster field and red-clump populations. We show our results in Supplementary Figure 15. As expected from the Δhk distributions, the signs of multiple stellar populations persist in our MDFs for most GCs.

Finally, cautions are advisable on our MDFs of GCs. Our metallicity scale is not on the traditional Zinn & West¹⁴ scale, therefore our MDFs for GCs can be different from those from other photometric or spectroscopic studies. RGB stars in ω Cen of Johnson *et al.* have different individual elemental abundances, which were not taken into consideration in our $[\text{Fe}/\text{H}]_{\text{spec}}$ versus $[\text{Fe}/\text{H}]_{\text{hk}}$ or $[\text{Ca}/\text{H}]_{\text{spec}}$ versus $[\text{Fe}/\text{H}]_{\text{hk}}$ relations. Furthermore, each GCs may have slightly different elemental abundance ratios and our calibrated photometric metallicities for GCs would be affected. However, it should be emphasized that the crux of our results is the split or the spread in the hk index in the RGB stars of individual GCs, which is insensitive to other elemental abundances except calcium as will be discussed below.

4 The Influence of Elemental Abundances on the hk Index

The realistic modeling of the resonance Ca II H & K lines requires proper understanding of stellar atmospheres, including chromospheres, and hydrodynamic non-local thermodynamic equilibrium treatments, which have posed difficult problems for decades⁴¹. Here, we demonstrate that the calcium abundance is the major factor that determines the hk index of RGB stars using 1-dimensional plane-parallel stellar atmospheres⁴².

Calcium Using the model atmosphere for the RGB star at the magnitude level of the horizontal branch with $T_{\text{eff}} = 4750$ K, $\log g = 2.0$ (in cgs unit), $v_{\text{turb}} = 2.0$ km/s, $[\text{Fe}/\text{H}] = -1.6$, we calculate synthetic spectra for $[\text{Ca}/\text{Fe}] = 0.25, 0.30, 0.35, 0.40, 0.45$ and we show some of our synthetic spectra in Supplementary Figure 17. We convolve the filter transmission functions with synthetic spectra and we obtain the calcium abundance sensitivity on the hk index, $\partial(hk)/\partial[\text{Ca}/\text{H}] \approx 0.422$ mag/dex. Note that this result is based on the fixed model parameters, such as T_{eff} , $\log g$, v_{turb} , and $[\text{Fe}/\text{H}]$, except calcium abundance. To interpret observed Δhk between the two stellar populations in a GC in terms of different calcium abundances, proper atmospheric parameters should be taken into consideration. For example, the two stellar groups with different $[\text{Fe}/\text{H}]$ and $[s\text{-process}/\text{Fe}]$

ratios in M22 by Marino *et al.*⁶ have slightly different elemental abundances and temperatures. The stars in the metal-poor group by Marino *et al.* have $\langle[\text{Fe}/\text{H}]\rangle = -1.82$, $\langle[\text{Ca}/\text{Fe}]\rangle = +0.25$ and those in the metal-rich group have $\langle[\text{Fe}/\text{H}]\rangle = -1.68$, $\langle[\text{Ca}/\text{Fe}]\rangle = +0.35$. The mean temperature of the stars in the metal-poor group is $\sim 100 \pm 42$ K hotter than those in the metal-rich group. Using these atmospheric parameters, we obtain $\Delta hk = 0.121 \pm 0.072$ mag, which is apparently consistent with the double peaks in the Δhk distribution of M22 within the error as shown in Supplementary Figure 7.

Helium As shown in Supplementary Figure 5, helium is very important in stellar structure and evolution. Very unfortunately, however, there is no direct method to measure helium abundances of stars in GCs. As we discussed, all the GCs with signs of multiple stellar populations have relatively EHB, for example, the second generation of the stars in M22 is expected to have enhanced helium abundance by $\Delta Y \approx 0.05$ inferred from its EHB morphology. Using the model atmospheres with enhanced helium abundance ($Y \approx 0.35$, equivalent to $\Delta Y \approx 0.10$) by Castelli³, we obtain $\Delta hk \approx -0.002$ mag, in the sense that the hk index decreases as helium abundance increases, and thus the effect of enhanced helium abundance on the hk index is negligible. Given the cool temperatures of RGB stars in GCs, the helium enhancement by $\Delta Y = 0.05 - 0.10$ does not appear to be important.

CNO It is well-known fact that many GCs show large star-to-star elemental abundance variations. In particular, almost all GCs show variations in the CNO abundances resulted from the internal evolutionary mixing accompanied with the CNO-cycle or the primordial pollution by intermediate-mass AGB stars to the second generation of the stars^{43,44}. In spite of their high abundances, the CNO abundances are hard to measure in the optical wavelength mainly due to the lack of atomic transitions. On the other hand, in the form of molecules, the CNO can affect the hk index, in particular the CN band at $\lambda 3885 \text{ \AA}$ as shown in Supplementary Figure 1. Both carbon and nitrogen contribute in the formation of CN molecules. The typical RGB stars in GCs show an anticorrelation between the CN band and the CH band strengths and a correlation between the CN band and the NH band strengths, indicating that the nitrogen controls the CN band strength⁴⁵. Our results suggest that the variations in the CNO abundances do not affect the hk index significantly. We obtain $\Delta hk \approx -0.007, +0.002, -0.004$ for $\Delta[\text{C,N,O}/\text{Fe}] = +1.0$ dex, respectively, and their influence on the hk index appears to be negligible.

Aluminium It is also well-known fact that many GCs show large star-to-star aluminium variations by more than $\Delta[\text{Al}/\text{Fe}] \approx 1.0$ dex, presumably resulted from the proton-capture process at high temperature or the primordial pollution by intermediate-mass AGB stars to the second generation of the stars^{44,46}. The resonance lines of Al I at $\lambda 3944.01$ and 3961.52 \AA are often very strong (see Supplementary Figure 17) and it may affect our conclusions that the hk index traces calcium abundances of RGB stars in GCs. We obtain $\Delta hk \approx 0.013$ mag for $\Delta[\text{Al}/\text{Fe}] = +1.0$ dex. The effect of the variations in aluminium abundances on the hk index is insignificant compared to our observations, by more than a factor of ten. The insignificant influence of aluminium on the Ca II

³<http://wwwuser.oat.ts.astro.it/castelli/grids.html>

H & K lines was also confirmed by others for the globular cluster NGC6752¹⁷.

α -elements The α -elements (O, Ne, Mg, Si, S, Ar, Ca, and Ti) are quite abundant and they are major donors to the H⁻ opacity in RGB stars. However, their influence, except for Ca, on the hk index appears to be small. We obtained $\Delta hk \approx -0.008$ mag for +0.3 dex variation in α -elements excluding calcium.

s -process elements RGB stars in GCs show large star-to-star s -process elemental abundance variations presumably resulted from the primordial pollution by intermediate-mass AGB stars to the second generation of the stars^{9,44}. For example, globular clusters M22 and NGC1851 show bimodal s -process elemental abundance distributions with $\Delta[s\text{-process/Fe}] \geq 0.5$ dex. We obtained $\Delta hk \approx +0.008$ mag for $\Delta[s\text{-process/Fe}] = +0.5$ dex, and thus their influence on the hk index is small.

28. Clarke, D., McLean, I. S. & Wyllie, T. H. A. Stellar Line Profiles by Tilt-scanned Narrow Band Interference Filters. *Astron. Astrophys. J.* **43**, 215–221 (1975).
29. Harris, W. E. Catalog of Parameters for Globular Clusters in the Milky Way. *Astron. J.* **112**, 1487–1488 (1996).
30. Hesser, J. E. *et al.* Strong CN stars in the globular cluster NGC 1851. *Astron. J.* **87**, 1470–1477 (1982).
31. Monaco, L. *et al.* Wide-field photometry of Galactic globular cluster M22. *Mon. Not. R. Astron. Soc.* **349**, 1278–1290 (2004).
32. Beers, T. C. Estimation of the equivalent width of the interstellar Ca II K absorption line. *Astron. J.* **99**, 323–329 (1990).
33. Hunter, I. *et al.* Early-type stars observed in the ESO UVES Paranal Observatory Project – I. Interstellar Na I UV, Ti II and Ca II K observations. *Mon. Not. R. Astron. Soc.* **367**, 1478–1514 (2006).
34. Andrews, S. M., Meyer, D. M. & Lauroesch, J. T. Small-scale interstellar Na I structure toward M92. *Astron. J.* **99**, 323–329 (1990).
35. Smoker, J. V. *et al.* Ca II K interstellar observations towards early-type disc and halo stars, abundances and distances of intermediate- and high-velocity clouds.. *Mon. Not. R. Astron. Soc.* **367**, 1478–1514 (2006).
36. Piotto, G. Observations of multiple populations in star clusters. *ArXiv Astrophysics e-prints* (2009). arXiv:astro-ph/0902.1422v1.
37. D’Antona, F., *et al.* Helium variation due to self-pollution among Globular Cluster stars. Consequences on the horizontal branch morphology. *Astron. Astrophys. J.* **395**, 69–75 (2002).

38. Carretta, E. *et al.* Na-O anticorrelation and HB. I. The Na-O anticorrelation in NGC 2808 *Astron. Astrophys. J.* **450**, 523–533 (2006).
39. Marino, A. F. *et al.* Spectroscopic and photometric evidence of two stellar populations in the Galactic globular cluster NGC 6121 (M 4) *Astron. Astrophys. J.* **490**, 625–640 (2008).
40. Carretta, E. *et al.* Na-O anticorrelation and horizontal branches. II. The Na-O anticorrelation in the globular cluster NGC 6752 *Astron. Astrophys. J.* **464**, 927–937 (2007).
41. Linsky, J. L. & Avrett, E. H. The Solar *H* and *K* Lines. *Pub. Astron. Soc. Pacif.* **82**, 169–248 (1970).
42. Castelli, F. & Kurucz, R. L. New Grids of ATLAS9 Model Atmosphere. *ArXiv Astrophysics e-prints* (2004). arXiv:astro-ph/0405087.
43. Kraft, R. P. Abundance Differences Among Globular-Cluster Giants: Primordial Versus Evolutionary Scenarios. *Pub. Astron. Soc. Pacific.* **113**, 553–565 (1994).
44. Yong, D. *et al.* A Large C+N+O Abundance Spread in Giant Stars of the Globular Cluster NGC 1851. *Astrophys. J. Lett.* **695**, L62–L66 (2009).
45. Briley, M. M. & Smith, G. H. NH-, CH-, and CN-band strengths in M5 and M13 bright red giants. *Pub. Astron. Soc. Pacific.* **105**, 1260–1268 (1993).
46. Kraft, R. P. *et al.* Proton Capture Chains in Globular Cluster Stars. II. Oxygen, Sodium, Magnesium, and Aluminum Abundances in M13 Giants Brighter than the Horizontal Branch. *Astron. J.* **113**, 279–295 (1997).

	Uncertainty on the hk index	Note
Photometry	≤ 0.020 mag	random
Shifted CTIO $C\alpha$ passband	< 0.011 mag	systematic
Mean radial motion of GCs	< 0.006 mag	systematic
Internal velocity dispersion	< 0.001 mag	random
Interstellar Ca II absorption	< 0.010 mag	random
total	≤ 0.024 mag	
total (random)	≤ 0.022 mag	

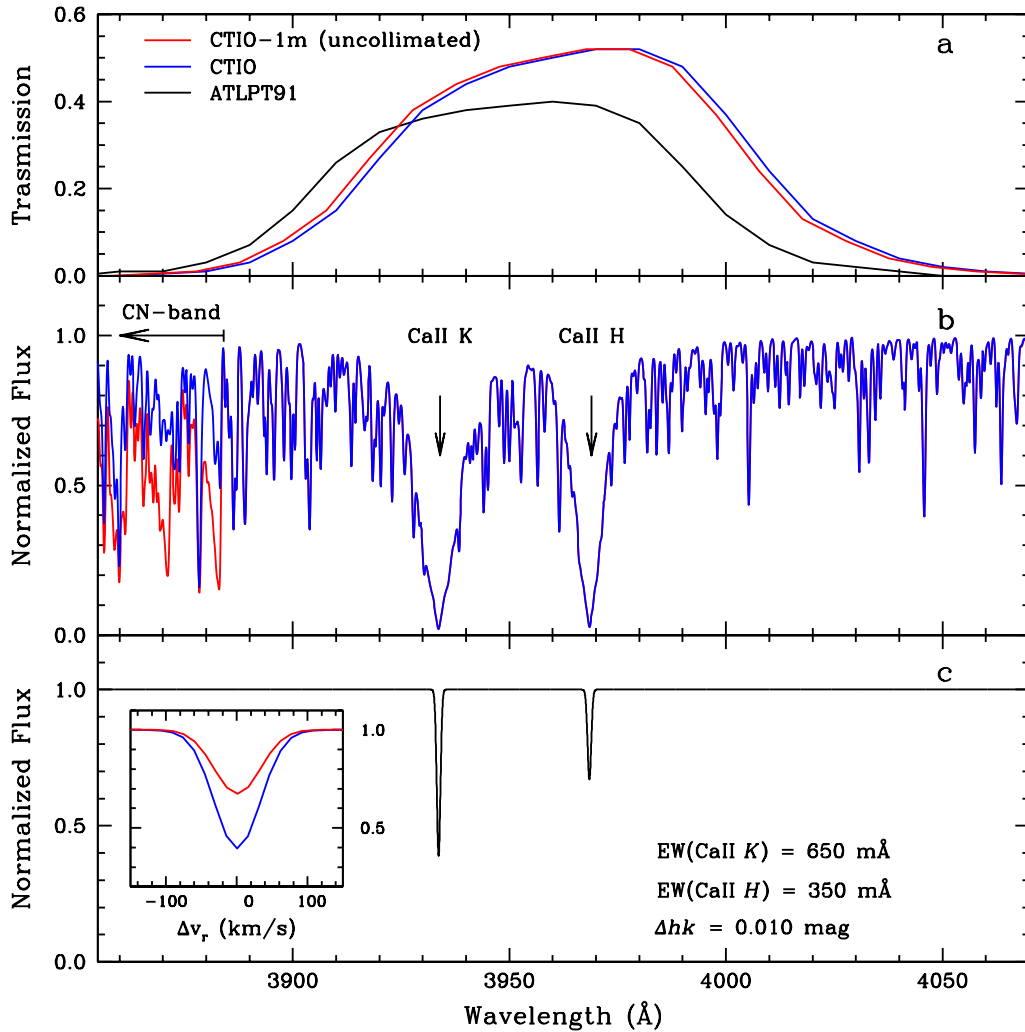
Supplementary Table 1: Summary of uncertainties relevant to the hk index.

ID	V_{HB}	$E(B - V)$	Exposure Time (sec)					Obs. Pos.		Date (MM/YY)
			Ca	u	v	b	y	RA	DEC	
ω Cen	14.53	0.12	12,860	4,890	2,130	1,300	13:26:44	-47:26:28	05/07, 02/08
M22	14.15	0.34	8,100	2,400	1,200	2,530	1,500	18:36:29	-23:55:34	07/08, 08/08
NGC1851	16.09	0.02	19,100	12,300	7,400	7,100	3,810	5:14:14	-40:01:49	02/08, 08/08
NGC2808	16.22	0.22	10,820	3,600	4,960	3,080	9:11:57	-64:49:24	05/07
M4	13.45	0.36	8,400	5,400	5,570	2,920	2,060	16:23:33	-26:30:47	05/07, 08/08
M5	15.07	0.03	9,660	3,900	2,100	4,010	2,390	15:18:29	2:04:03	05/07, 08/08
NGC6752	13.70	0.04	7,500	2,400	1,800	2,400	1,200	19:10:57	-60:00:20	07/08, 08/08
NGC6397	12.87	0.18	3,560	3,560	2,140	1,355	930	17:40:52	-53:36:06	08/06, 09/07

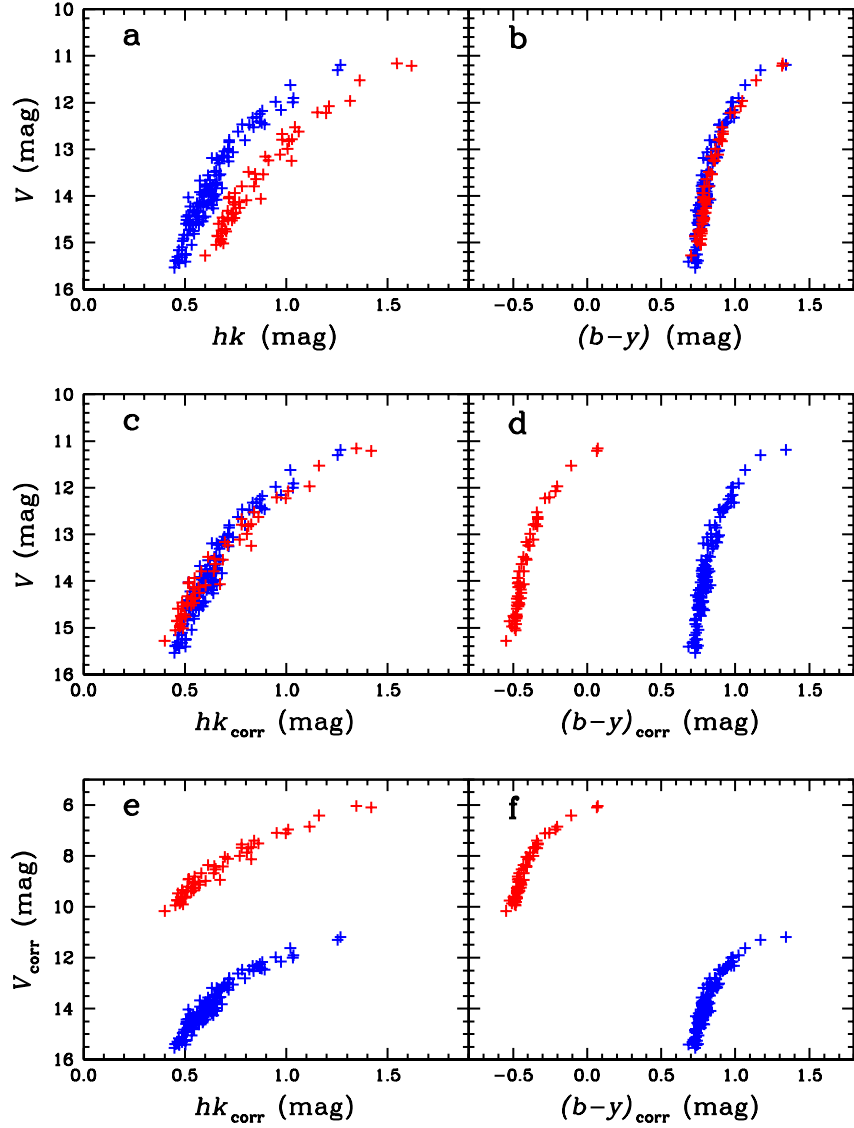
Supplementary Table 2: Journal of observations for eight GCs. Only one field has been observed for a particular GC and the coordinates are given in columns (9) and (10).

ID	FWHM(GB)		Measurement errors		Differential Reddening	
	$(b - y)$	hk	$\sigma_*(b - y)$	$\sigma_*(hk)$	$E(b - y)_{1/2}$	$E(hk)_{1/2}$
ω Cen	0.079	0.534	0.012	0.020	0.089	0.014
M22	0.050	0.216	0.004	0.008	0.252	0.041
NGC1851	0.035	0.182	0.006	0.013	0.015	0.002
NGC2808	0.042	0.159	0.008	0.019	0.163	0.026
M4	0.037	0.119	0.005	0.010	0.266	0.043
M5	0.025	0.105	0.006	0.013	0.022	0.004
NGC6752	0.022	0.090	0.004	0.007	0.030	0.005
NGC6397	0.024	0.034	0.007	0.012	0.133	0.022

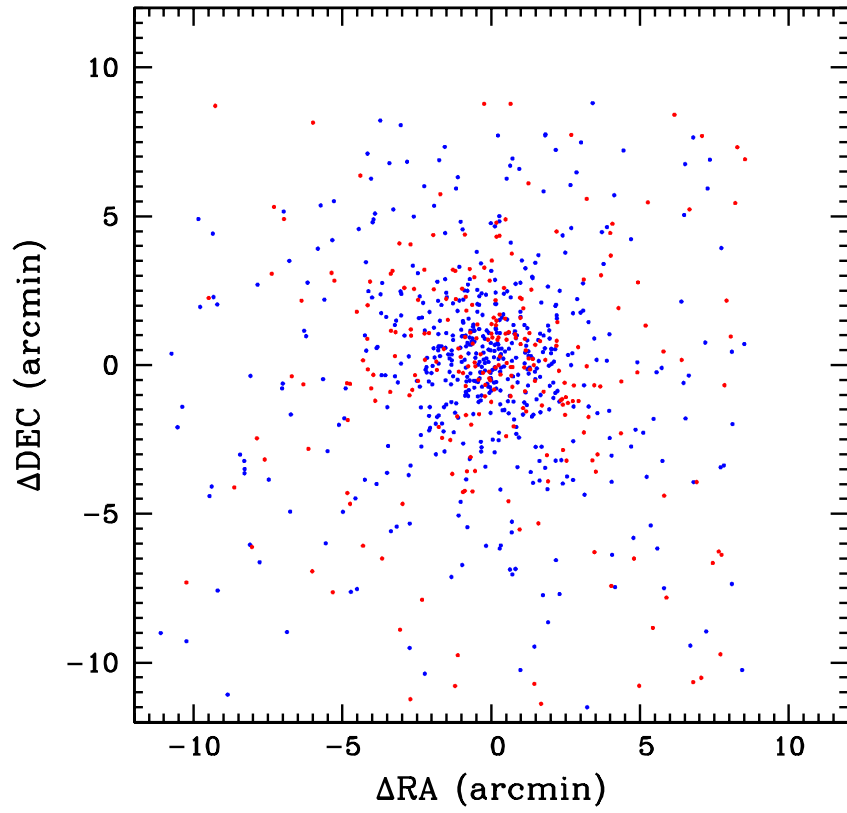
Supplementary Table 3: Comparisons of the observed FWHMs of RGB stars and the measurement errors at the magnitude level of horizontal branch stars, $V_{HB} + 0.5 \geq V \geq V_{HB} - 0.5$. The measurement errors are those for individual stars and, therefore, measurement errors for individual subpopulation in GCs will be given by $\approx \sigma_*(b - y)/\sqrt{n_p}$ or $\sigma_*(hk)/\sqrt{n_p}$, where n_p (≥ 20) is the number of stars in each subpopulation in GCs. Note that, while the FWHMs of most GCs have much larger values [$\geq 8\sigma_*(hk)$] than the measurement errors for individual stars in the hk index, the FWHM of NGC6397 is comparable in size to the measurement error in the hk index, consistent with the idea that NGC6397 is the only normal GC in our sample (see Supplementary Figures 6 –13). The last two columns, $E(b - y)_{1/2}$ and $E(hk)_{1/2}$, denote contributions due to the differential reddening effect assuming a 50% variation in the total interstellar reddening of each GC, with which observed FWHMs of GCs in the $(b - y)$ color and in the hk index can not be explained simultaneously.



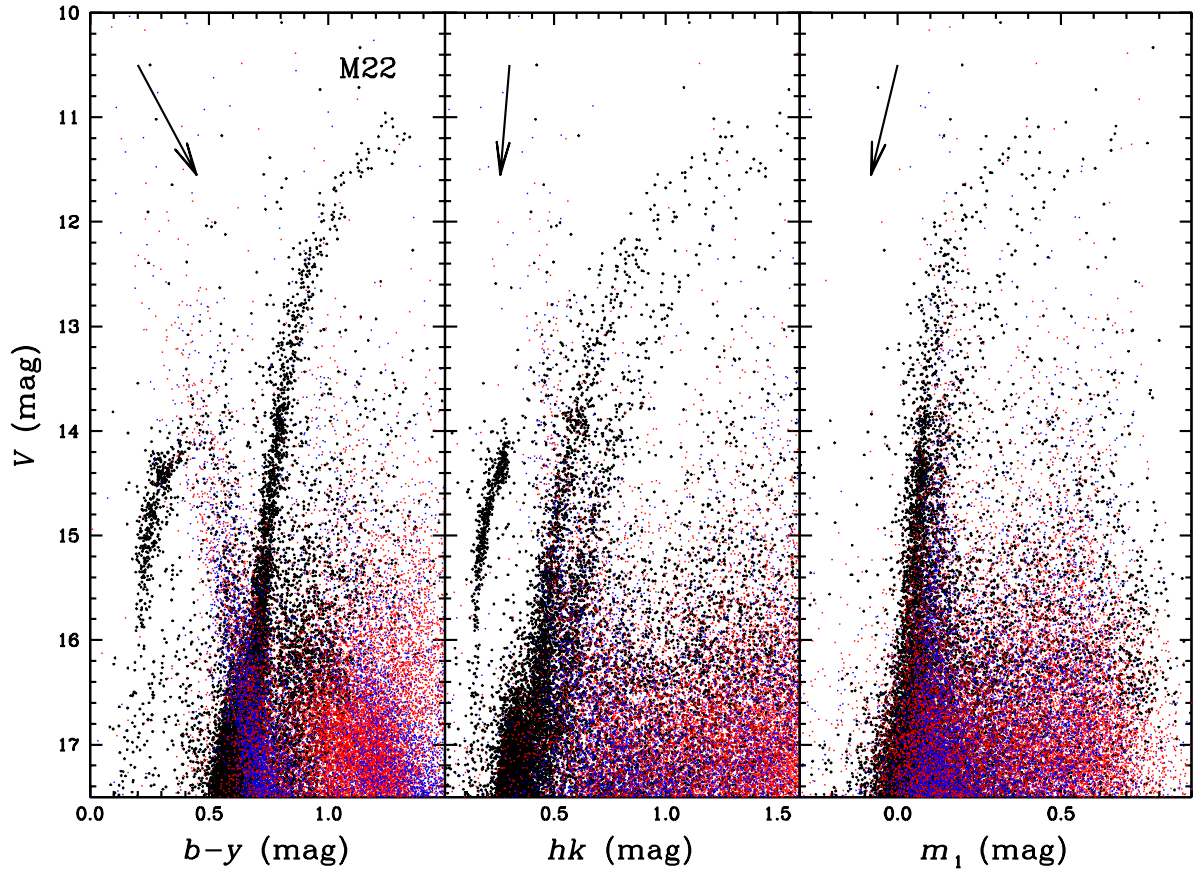
Supplementary Figure 1: (a) A comparison of *Ca* filter transmission functions between that in Anthony-Twarog *et al.*¹² (the black line) and that for the CTIO 1-m telescope (the blue line). Both filters have similar FWHMs, approximately 90 Å, but the passband for the CTIO 1-m telescope is shifted approximately 15 Å to the longer wavelength. (b) Synthetic spectra for the CN normal (the blue line) and the CN strong (the red line) RGB stars. The CN band at λ 3885 Å lies on the lower tail of the *Ca* filter but the contamination from the CN band is insignificant. (c) Synthetic spectra for the interstellar Ca II *H* & *K* lines. We adopt equivalent widths of 350 mÅ and 650 mÅ for the interstellar Ca II *H* & *K* lines, respectively, with a gaussian line profile with a FWHM of 1 Å (equivalent to $\Delta v_r \approx 76$ km/s). In the inset of the figure, the red line denotes the velocity profile for the interstellar Ca II *H* line and the blue line for the interstellar Ca II *K* line. This large amount of discrete interstellar absorption contributes only 0.010 mag to our results.



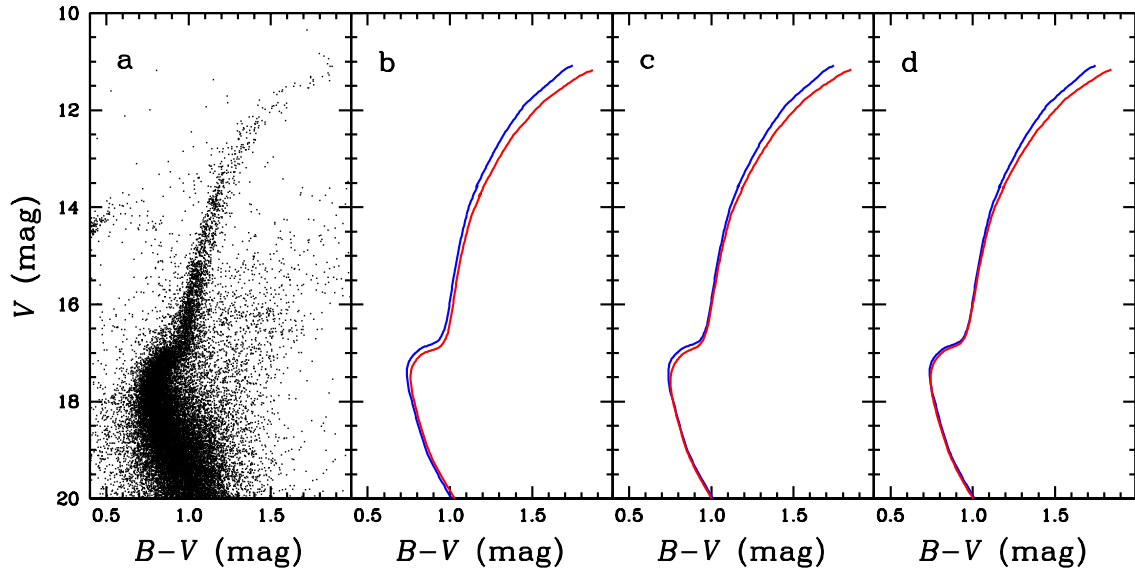
Supplementary Figure 2: (a & b) Blue crosses and red crosses denote RGB stars in the Ca-w and the Ca-s groups, respectively, with proper motion membership probabilities $P \geq 90\%$. (c) RGB stars in the Ca-s group are shifted by $\Delta hk = -0.20$ mag to match with those in the Ca-w group, assuming the RGB split in M22 is due to differential reddening. The reddening correction value of $\Delta hk = -0.20$ mag for the Ca-s group is equivalent to $E(B - V) = -1.69$. (d) The RGB stars in the Ca-s group are shifted by $\Delta(b - y) = -1.25$ mag, assuming $E(b - y)/E(B - V) = 0.74$, and two RGB sequences do not agree, in the sense that RGB stars in the Ca-s group is too hot to be in the RGB phase. (e & f) After applying reddening correction in V ($= -5.24$ mag), assuming $A_V = 3.1 \times E(B - V)$. The RGB stars in the Ca-s group become too bright to be members of M22, inconsistent with the proper motion study of the cluster.



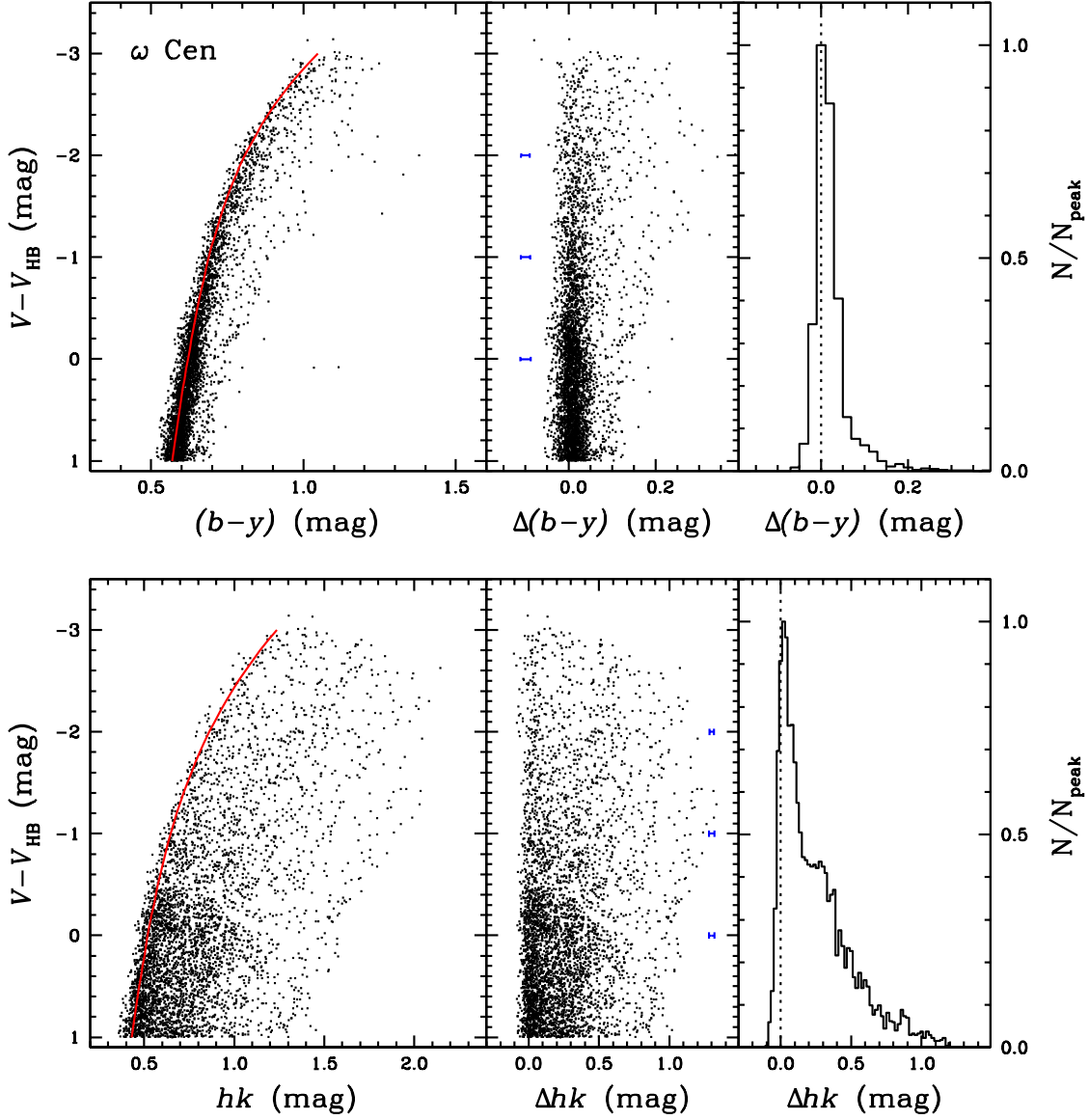
Supplementary Figure 3: Spatial distribution of the Ca-w (blue dots) and the Ca-s (red dots) groups in M22. Note the absence of spatially patched features, indicating that differential reddening is not responsible for the RGB split in M22.



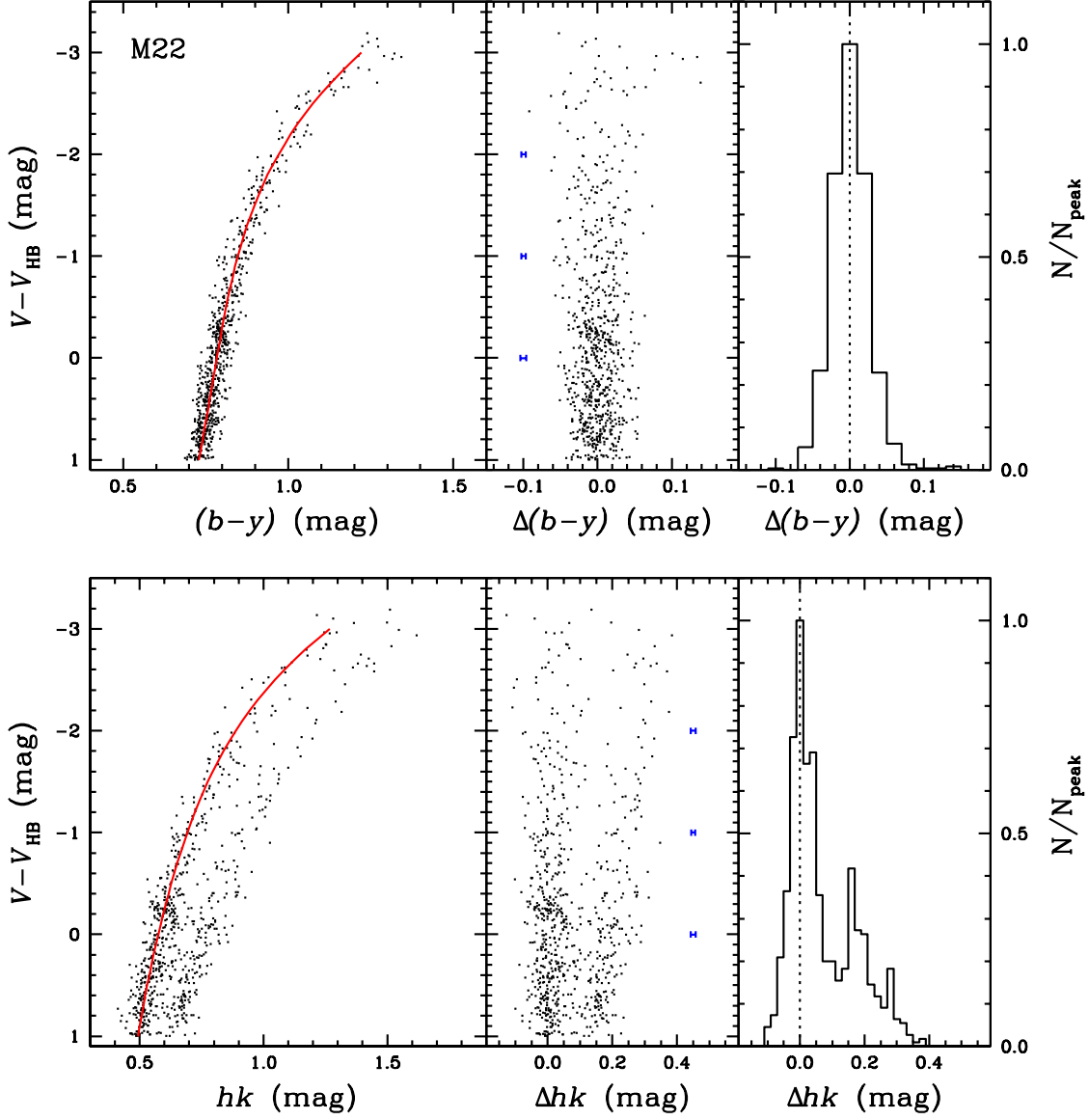
Supplementary Figure 4: Color-magnitude diagrams for M22 and two bulge fields (NGC6528 and OGLEII-12). The black dots represent M22, the red dots and the blue dots denote NGC6528 and OGLEII-12, respectively. The stars in the Milky Way bulge are fainter and redder than those in M22 are and they do not affect the double RGB sequences in M22. Black arrows indicate reddening vectors, assuming $E(B - V) = 0.34$ for M22²⁹.



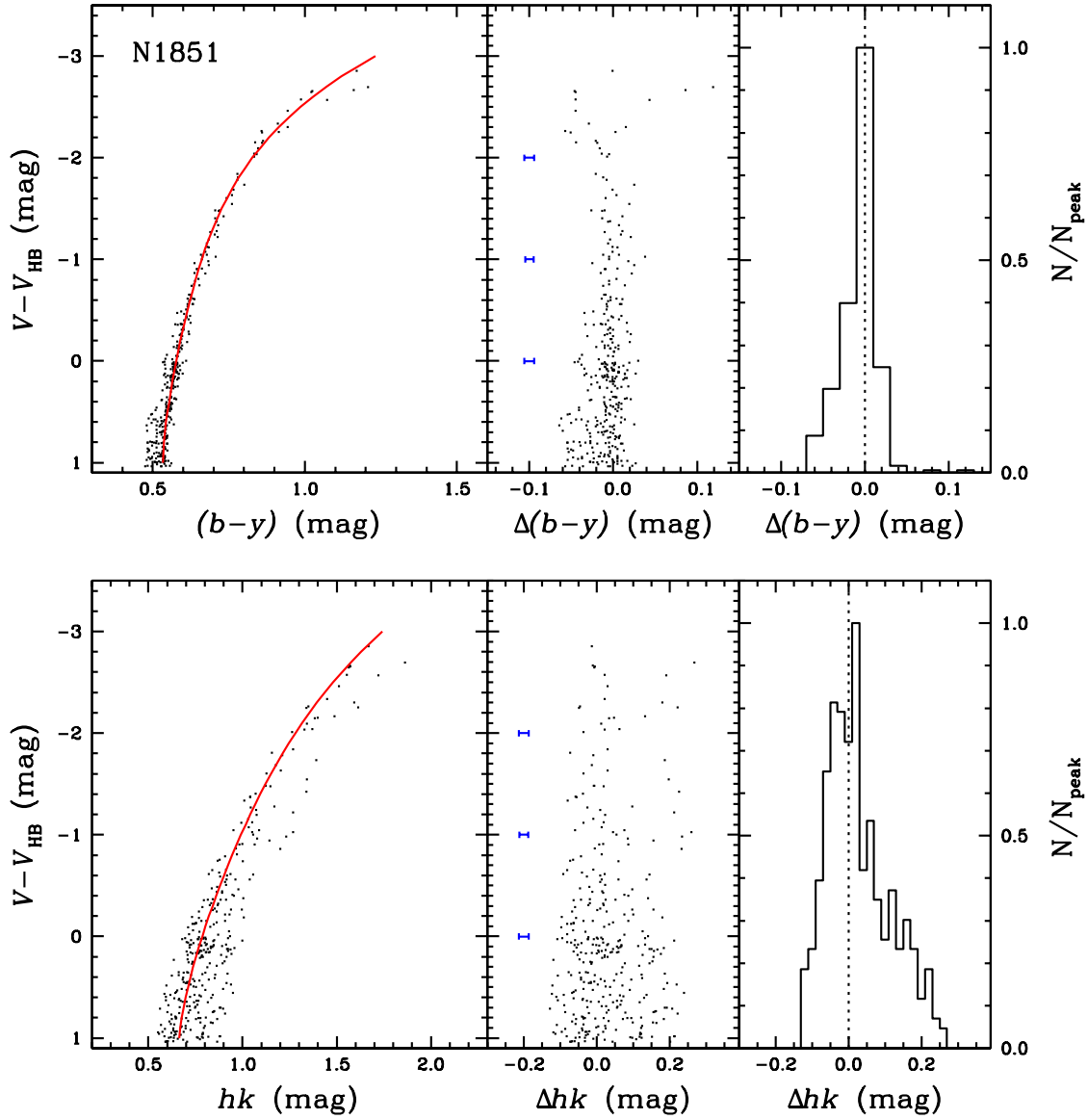
Supplementary Figure 5: (a) The color-magnitude diagram by Monaco *et al.*³¹ (b) Model isochrones for $[\text{Fe}/\text{H}] = -1.6$ (a blue line), and -1.4 (a red line), $Y = 0.23$, and 11 Gyr. (c) Model isochrones for $[\text{Fe}/\text{H}] = -1.6$, $Y=0.23$, 11 Gyr (a blue line) and $[\text{Fe}/\text{H}] = -1.4$, $Y=0.28$, 11 Gyr (a red line). (d) Model isochrones for $[\text{Fe}/\text{H}] = -1.6$, $Y=0.23$, 11 Gyr (a blue line) and $[\text{Fe}/\text{H}] = -1.4$, $Y=0.28$, 10 Gyr (a red line).



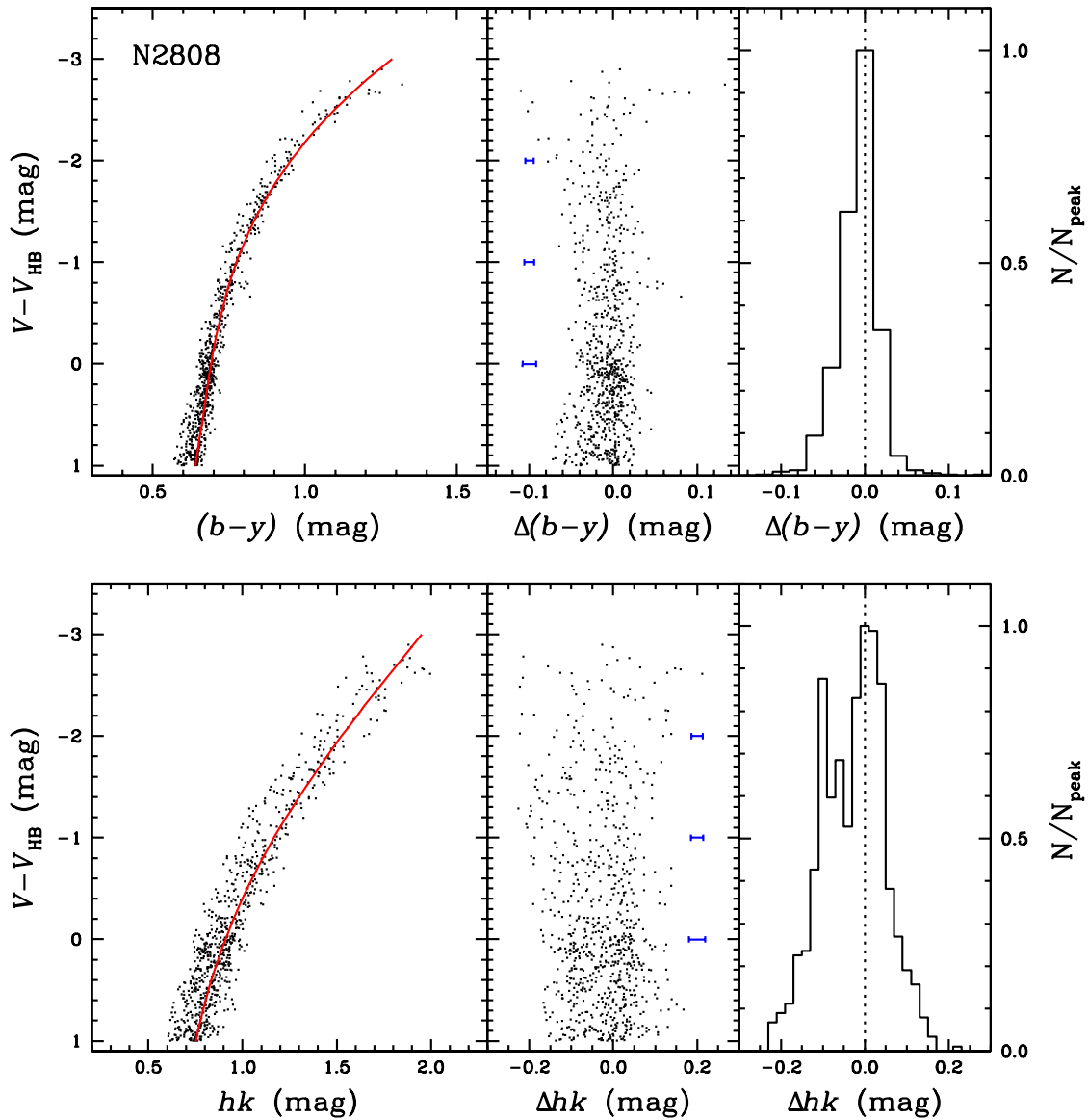
Supplementary Figure 6: The $(b - y)$ and hk distributions of RGB stars in ω Cen. The red lines denote fiducial sequences of the cluster, which are forced to pass through the peak $(b - y)$ colors or hk indices of given magnitude bins. The $\Delta(b - y)$ and the Δhk are differences in the $(b - y)$ color and the hk index, respectively, of each RGB stars from the fiducial sequences. The blue horizontal bars indicate measurement errors with a $2\sigma_*$ range ($\pm 1\sigma_*$) of individual stars at given magnitude bins. From the hk distribution, at least five distinct populations, whose hk splits are much larger than the measurement errors, can be found in ω Cen.



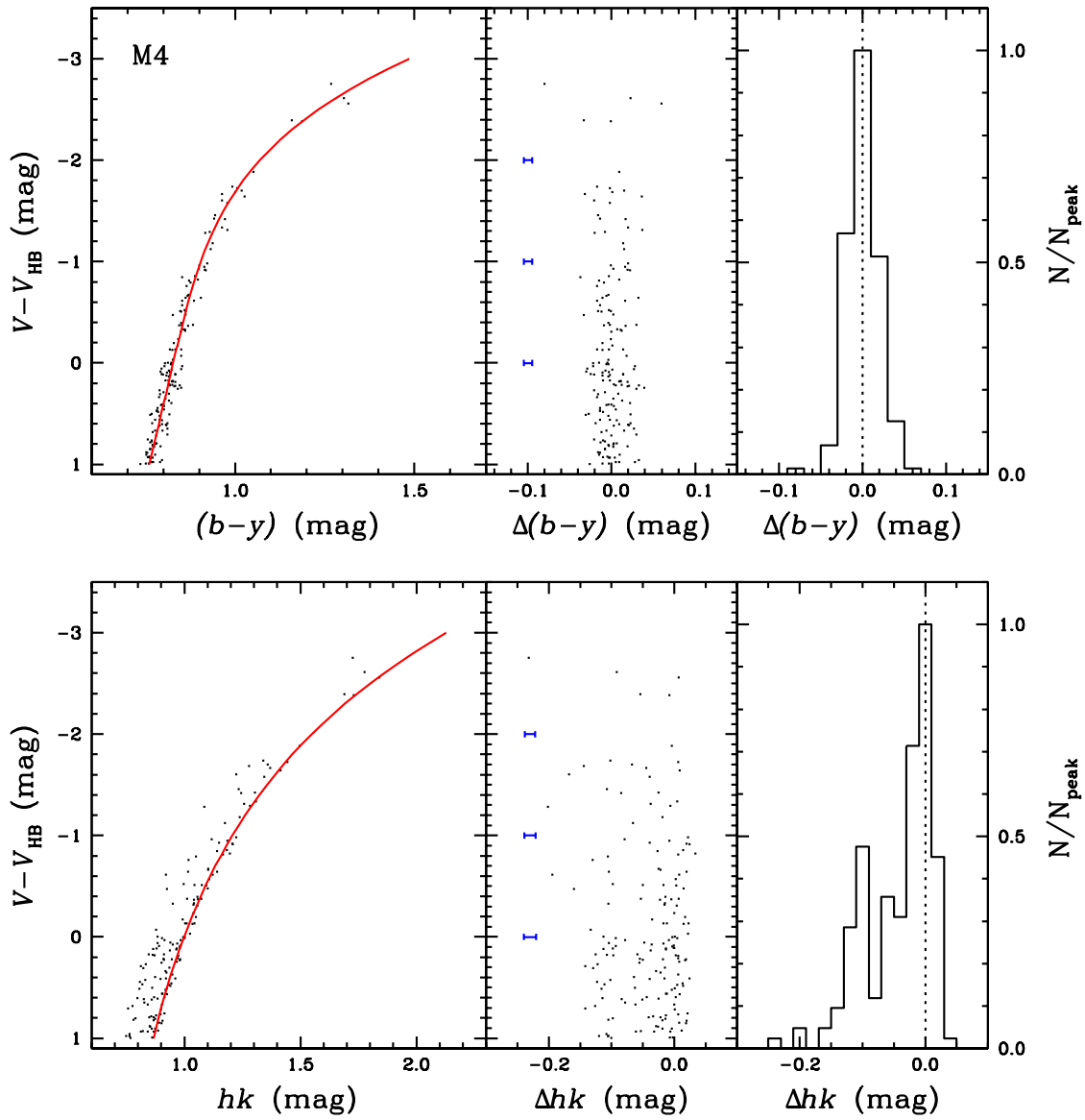
Supplementary Figure 7: The $(b - y)$ and hk distributions of RGB stars in M22. The blue horizontal bars indicate measurement errors with a $2\sigma_*$ range ($\pm 1\sigma_*$) of individual stars at given magnitude bins. Two distinct and discrete populations can be found in M22. At the magnitude of HB, the hk split between two populations is larger than $25 \times \sigma_*(hk)$ or $250 \times \sigma_p(hk)$, where $\sigma_*(hk)$ and $\sigma_p(hk)$ denote measurement errors for individual stars and populations in the hk index, respectively.



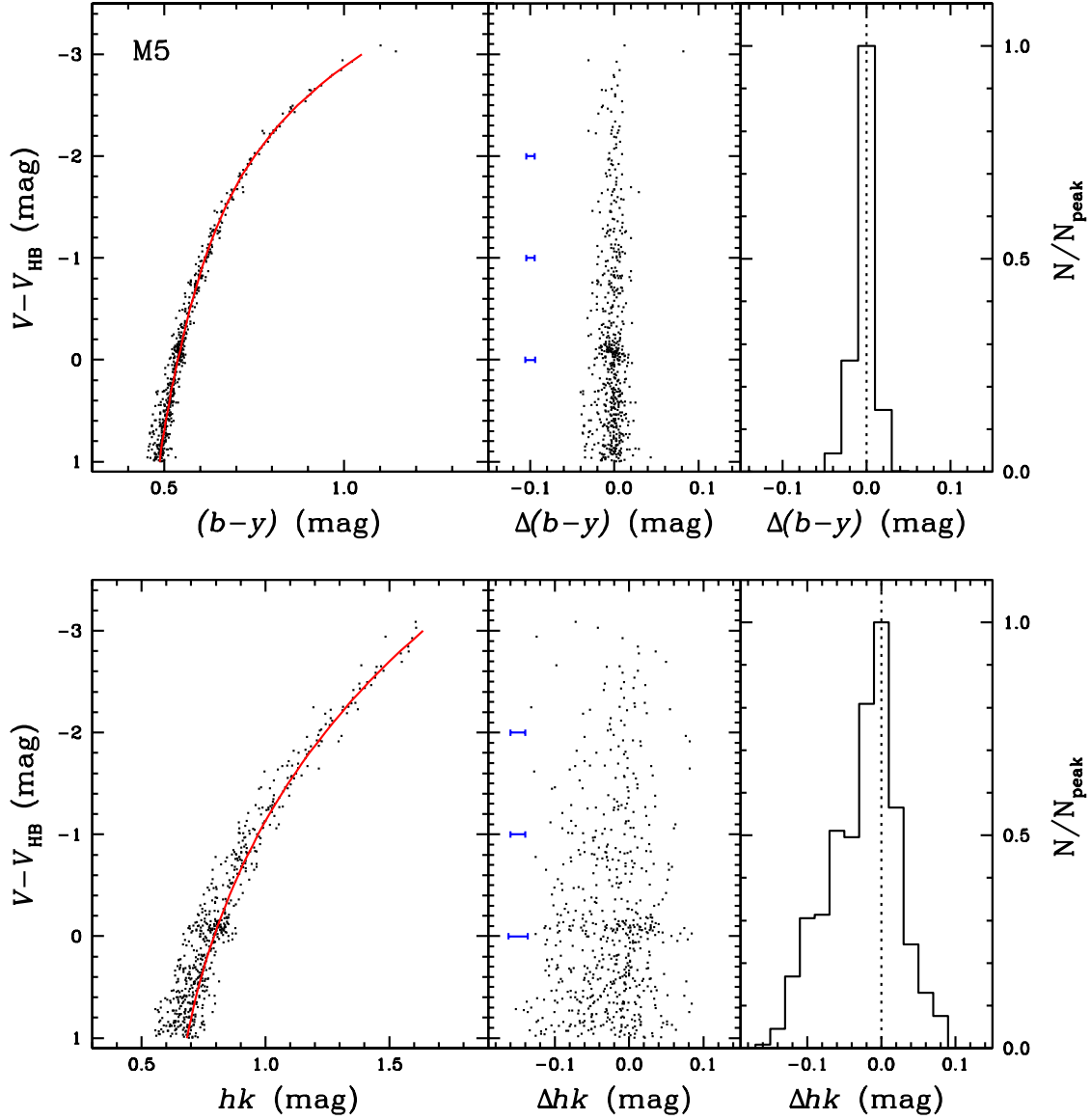
Supplementary Figure 8: The $(b - y)$ and hk distributions of RGB stars in NGC1851. The blue horizontal bars indicate measurement errors with a $2\sigma_*$ range ($\pm 1\sigma_*$) of individual stars at given magnitude bins. Two discrete populations can be found in NGC1851. At the magnitude of HB, the hk split between two populations is larger than $11 \times \sigma_*(hk)$ or $55 \times \sigma_p(hk)$.



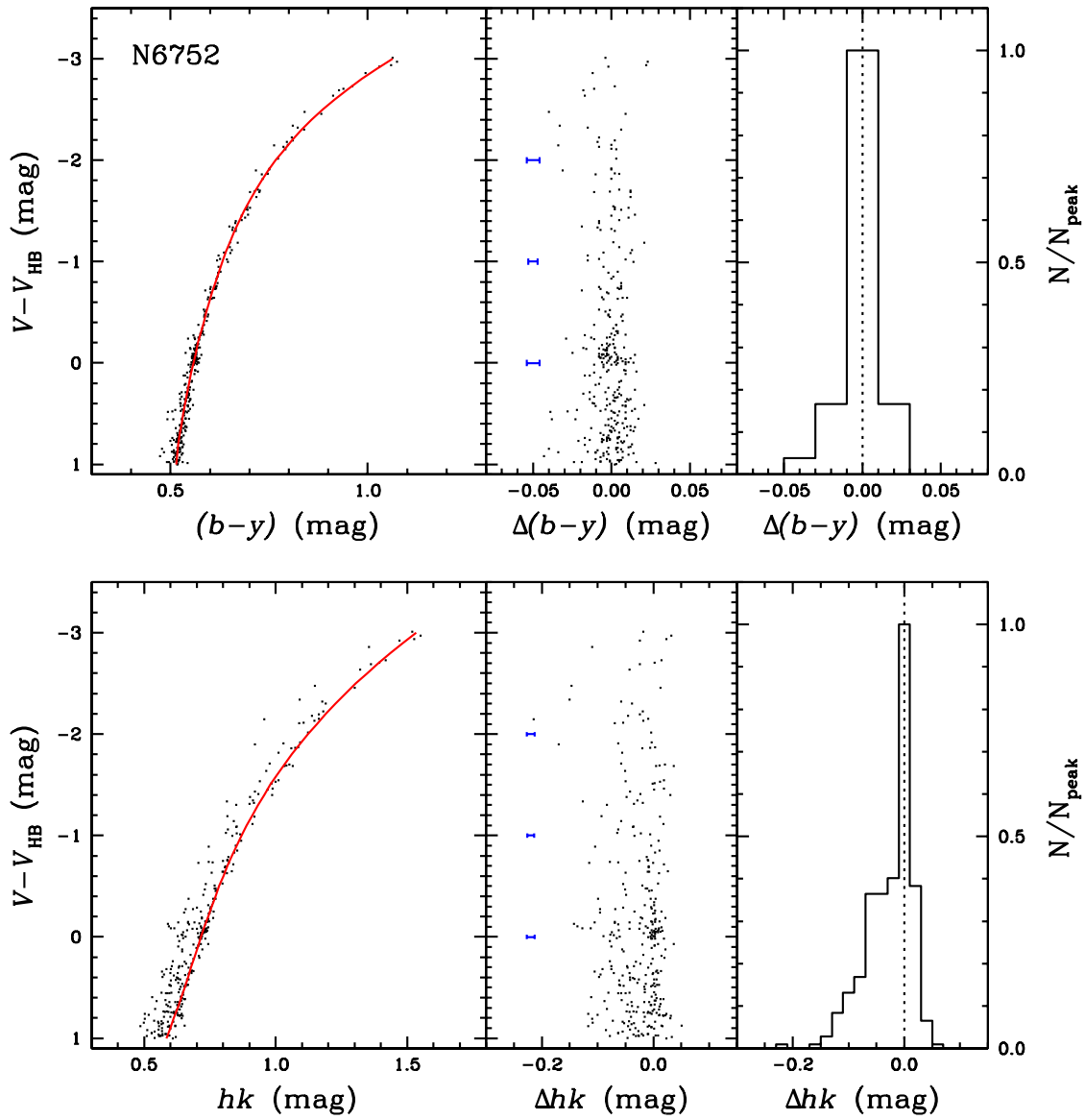
Supplementary Figure 9: The $(b - y)$ and hk distributions of RGB stars in NGC2808. The blue horizontal bars indicate measurement errors with a $2\sigma_*$ range ($\pm 1\sigma_*$) of individual stars at given magnitude bins. At least two discrete populations can be found in NGC2808. At the magnitude of HB, the hk split between two major populations is larger than $5 \times \sigma_*(hk)$ or $50 \times \sigma_p(hk)$.



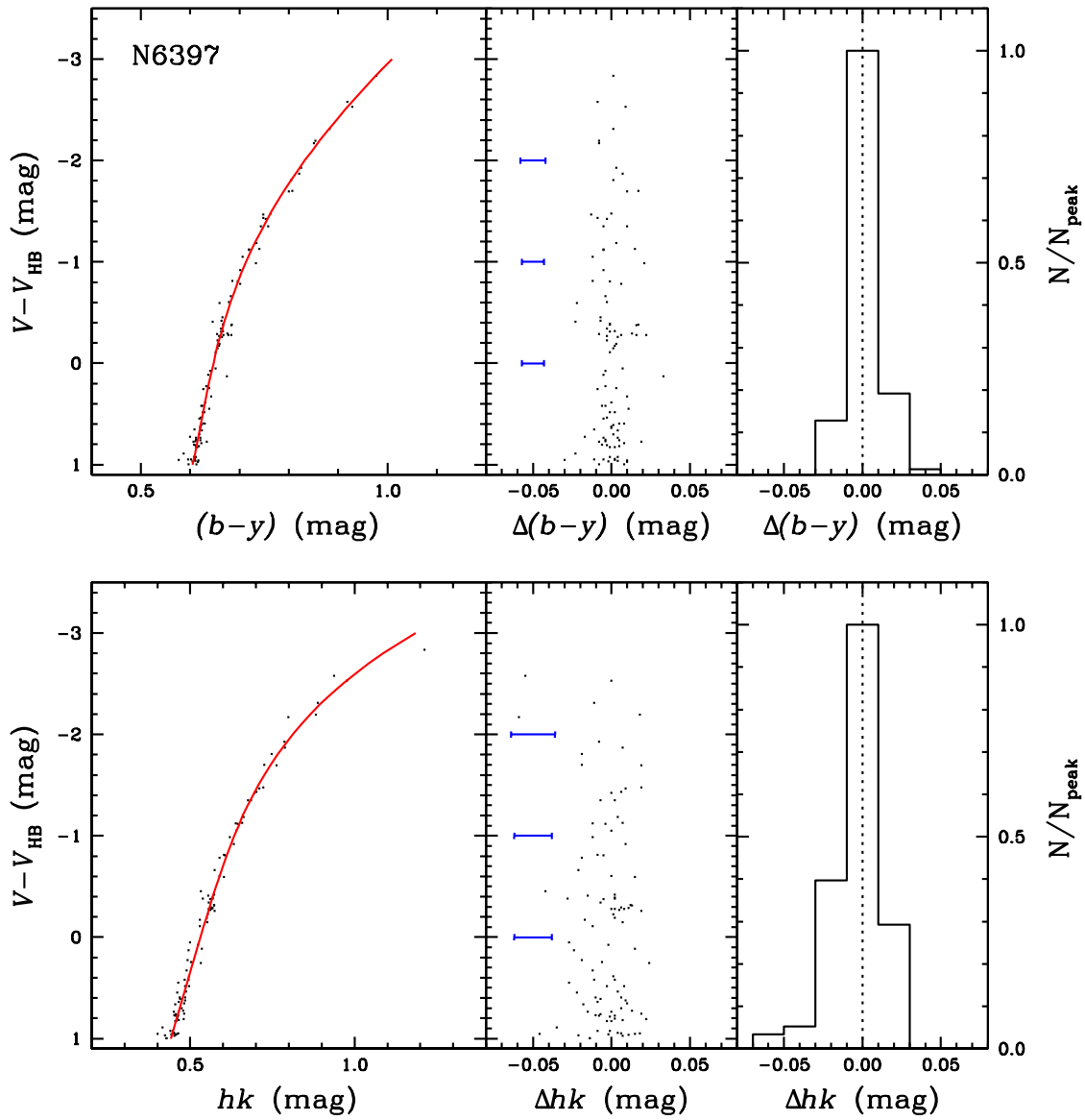
Supplementary Figure 10: The $(b - y)$ and hk distributions of RGB stars in M4. The blue horizontal bars indicate measurement errors with a $2\sigma_*$ range ($\pm 1\sigma_*$) of individual stars at given magnitude bins. Two discrete populations can be found in M4. At the magnitude of HB, the hk split between two populations is larger than $10 \times \sigma_*(hk)$ or $45 \times \sigma_p(hk)$.



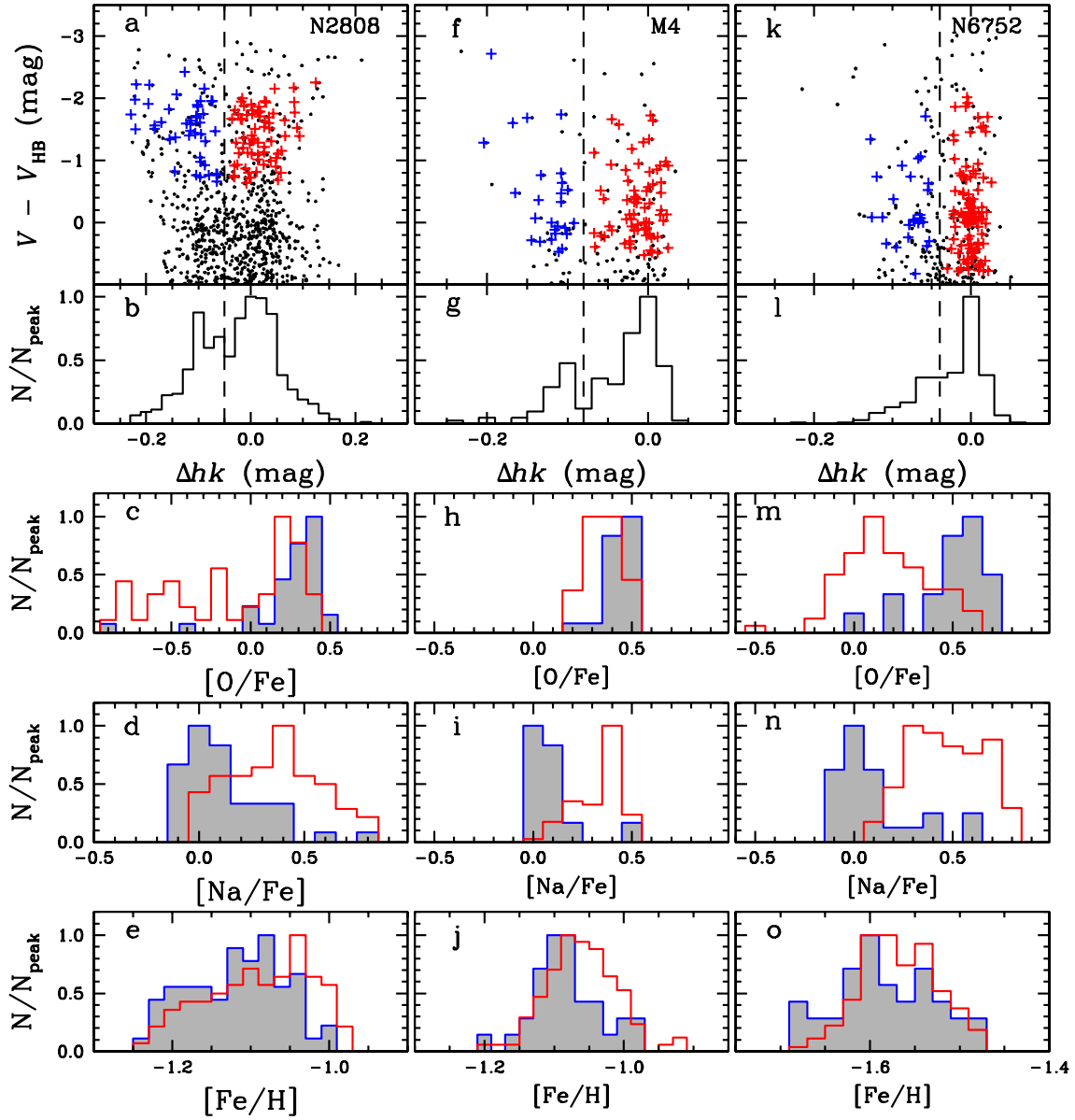
Supplementary Figure 11: The $(b - y)$ and hk distributions of RGB stars in M5. The blue horizontal bars indicate measurement errors with a $2\sigma_*$ range ($\pm 1\sigma_*$) of individual stars at given magnitude bins. The RGB sequence of the cluster shows a large spread in the hk index, indicative of heterogeneous calcium abundances. At the magnitude of HB, the FWHM of RGB stars in M5 is larger than $8 \times \sigma_*(hk)$.



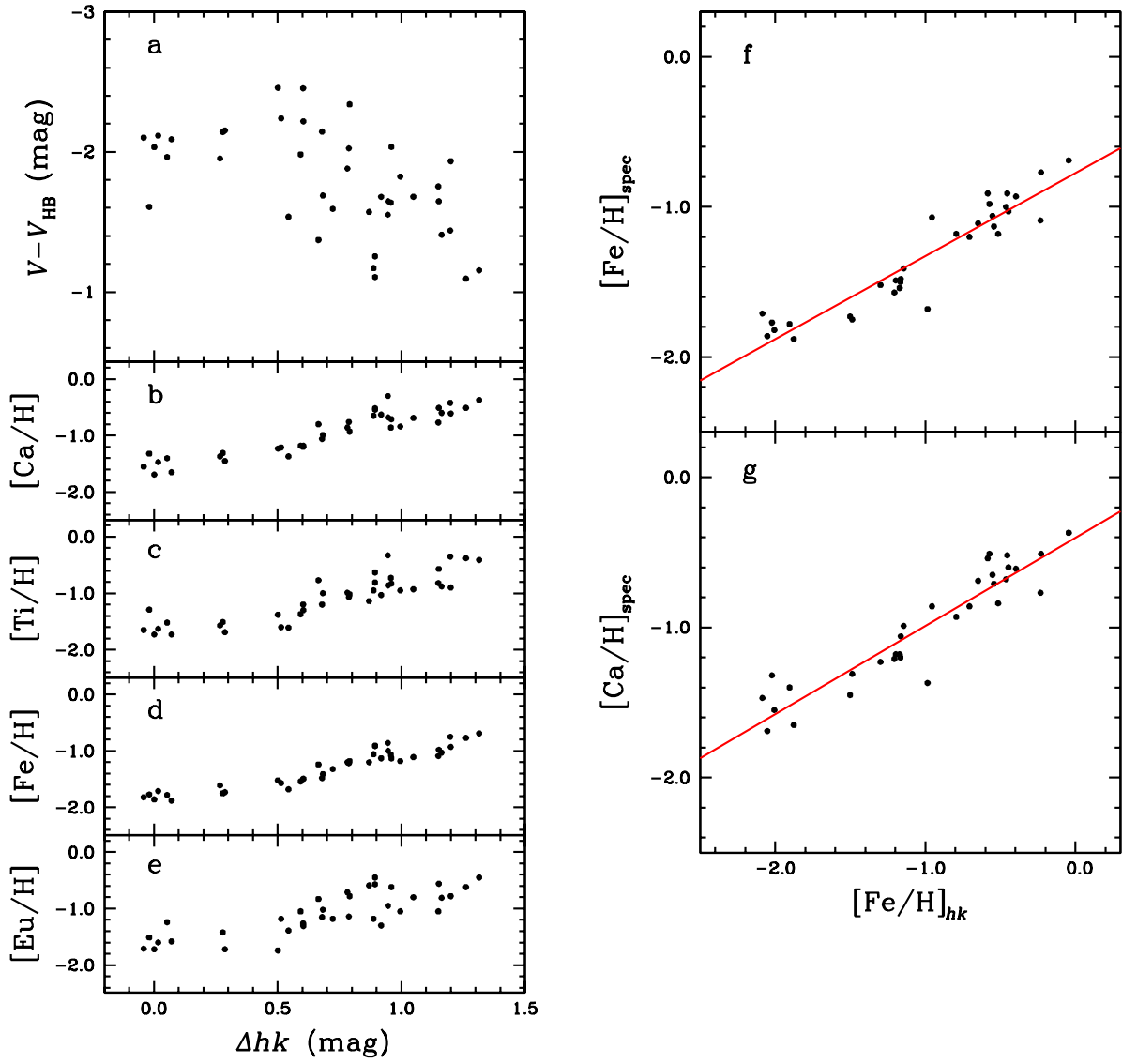
Supplementary Figure 12: The $(b - y)$ and hk distributions of RGB stars in NGC6752. The blue horizontal bars indicate measurement errors with a $2\sigma_*$ range ($\pm 1\sigma_*$) of individual stars at given magnitude bins. Two discrete populations can be found in NGC6752. At the magnitude of HB, the hk split between two populations is larger than $10 \times \sigma_*(hk)$ or $70 \times \sigma_p(hk)$.



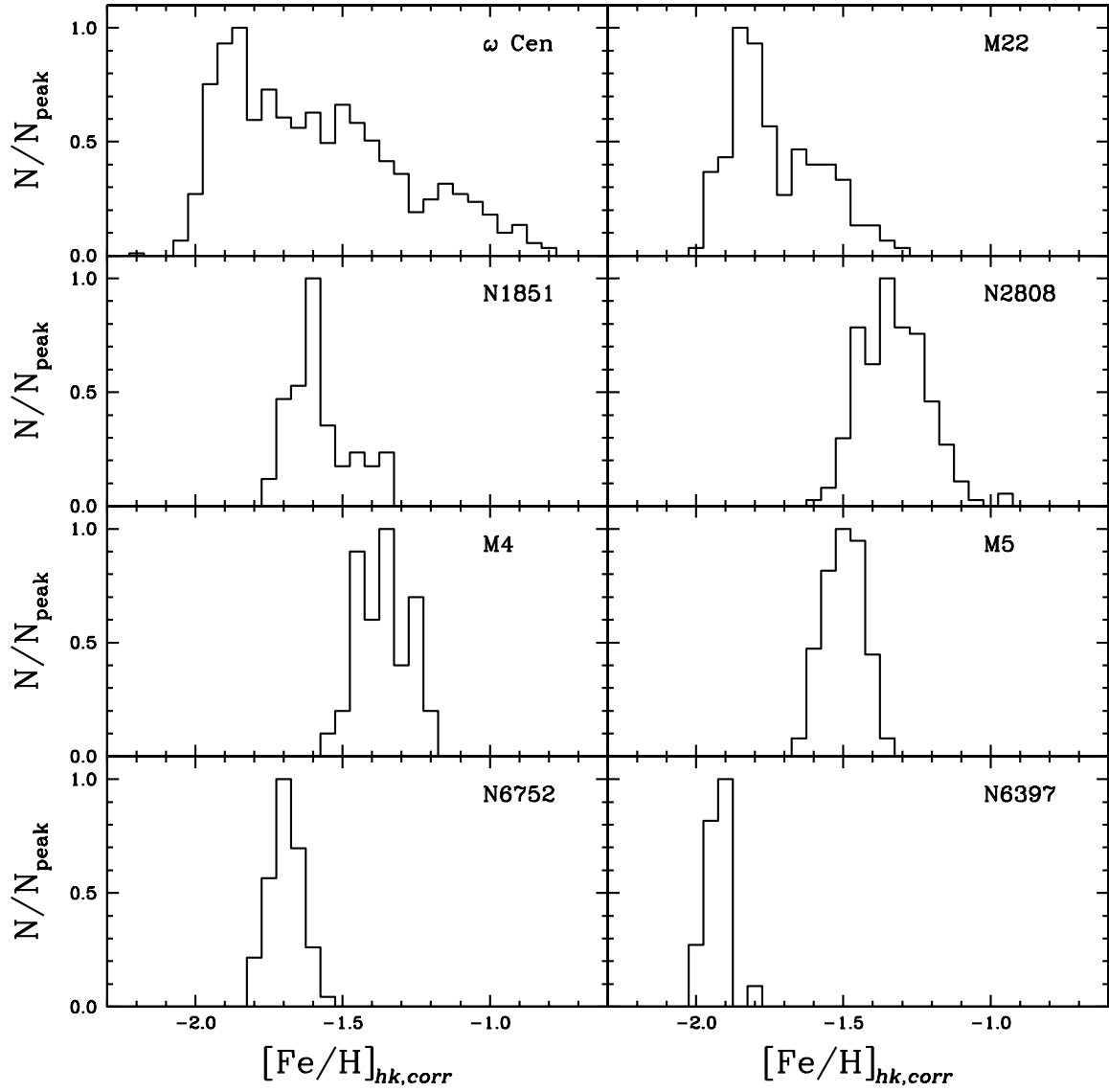
Supplementary Figure 13: The $(b - y)$ and hk distributions of RGB stars in NGC6397. The blue horizontal bars indicate measurement errors with a $2\sigma_*$ range ($\pm 1\sigma_*$) of individual stars at given magnitude bins. It is the only normal GC in Figure 2. Note the similar degree of the RGB widths in $\Delta(b - y)$ and Δhk and the similar degree of RGB widths as the measurement errors.



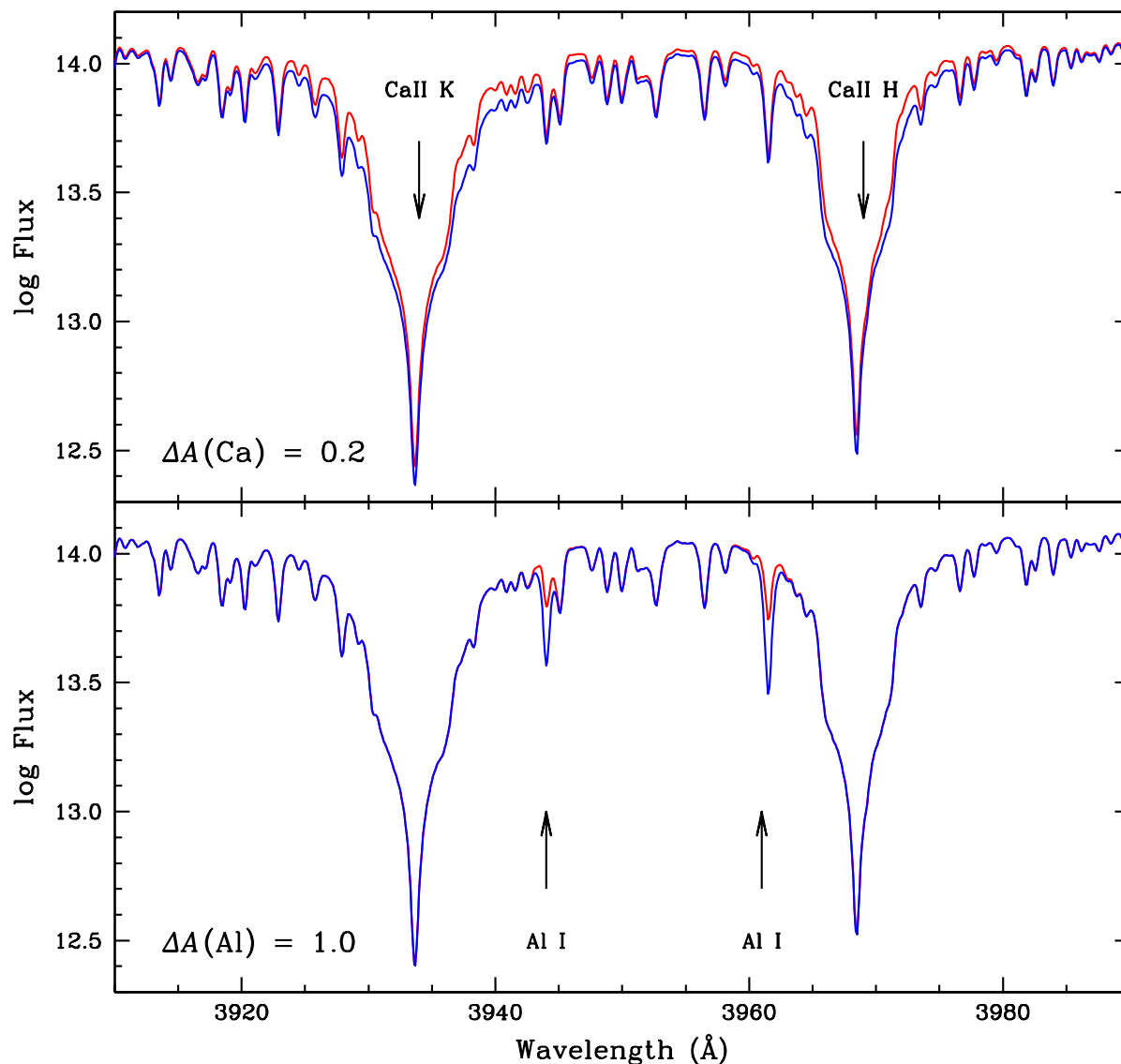
Supplementary Figure 14: (a) A plot of $V - V_{\text{HB}}$ versus Δhk for RGB stars in NGC2808. The blue and red plus signs denote the Ca-w and the Ca-s RGB stars. The dashed line denotes the boundary between the two groups at $\Delta hk = -0.05$ mag. (b) The Δhk distribution of NGC2808 RGB stars. (c) The $[\text{O}/\text{Fe}]$ distributions of the two RGB populations in NGC2808. The shaded histogram outlined with blue color is for the Ca-w group and the blank histogram outlined with red color is for the Ca-s group. (d) The $[\text{Na}/\text{Fe}]$ distributions. (e) The $[\text{Fe}/\text{H}]$ distributions. (f–j) Same as (a–e), but for M4 RGB stars with the boundary at $\Delta hk = -0.08$ mag. (k–o) Same as (a–e), but for NGC6752 RGB stars with the boundary at $\Delta hk = -0.04$ mag.



Supplementary Figure 15: (a) A plot of $V - V_{HB}$ versus Δhk for 40 RGB stars in ω Cen of Johnson et al.⁵ (b – e) Elemental abundances of 40 RGB stars in ω Cen as functions of Δhk . (f – g) Comparisons of our photometric metallicity, $[\text{Fe}/\text{H}]_{hk}$, with spectroscopic metallicity, $[\text{Fe}/\text{H}]_{\text{spec}}$, and calcium abundance, $[\text{Ca}/\text{H}]_{\text{spec}}$. The linear fits to the data are shown with red lines.



Supplementary Figure 16: Metallicity distribution functions for eight GCs derived from the hk index. In the figure, $[\text{Fe}/\text{H}]_{hk,corr}$ is our recalibrated photometric metallicity using the equation (4). Note that we only use bright RGB stars in order to minimize contamination from off-cluster field and red-clump populations. For most GCs, signs of multiple stellar populations persist in our MDFs.



Supplementary Figure 17: Comparisons of synthetic spectra for $[Fe/H] = -1.6$, $T_{\text{eff}} = 4750$ K, $\log g = 2.0$. (Upper panel) The red line denotes synthetic spectrum for $[Ca/Fe] = 0.25$ dex and the blue line denotes that for $[Ca/Fe] = 0.45$ dex. We adopt the fixed aluminium abundance of $[Al/Fe] = 0.50$ dex. (Lower panel) The red line denotes the synthetic spectrum for $[Al/Fe] = 0.00$ dex and the blue line denotes that for $[Al/Fe] = 1.00$ dex. We adopt the fixed calcium abundance of $[Ca/Fe] = 0.30$ dex. The effect of aluminium contamination on the hk index appears to be negligible.